

Composition of quasi-stationary solar wind flows from Ulysses/Solar Wind Ion Composition Spectrometer

R. von Steiger,^{1,2} N. A. Schwadron,¹ L. A. Fisk,¹ J. Geiss,² G. Gloeckler,^{1,3} S. Hefti,¹ B. Wilken,⁴ R. F. Wimmer-Schweingruber,⁵ and T. H. Zurbuchen¹

Abstract. Using improved, self-consistent analysis techniques, we determine the average solar wind charge state and elemental composition of nearly 40 ion species of He, C, N, O, Ne, Mg, Si, S, and Fe observed with the Solar Wind Ion Composition Spectrometer on Ulysses. We compare results obtained during selected time periods, including both slow solar wind and fast streams, concentrating on the quasi-stationary flows away from recurrent or intermittent disturbances such as corotating interaction regions or coronal mass ejections. In the fast streams the charge state distributions are consistent with a single freezing-in temperature for each element, whereas in the slow wind these distributions appear to be composed of contributions from a range of temperatures. The elemental composition shows the well-known first ionization potential (FIP) bias of the solar wind composition with respect to the photosphere. However, it appears that our average enrichment factor of low-FIP elements in the slow wind, not quite a factor of 3, is smaller than that in previous compilations. In fast streams the FIP bias is found to be yet smaller but still significantly above 1, clearly indicating that the FIP fractionation effect is also active beneath coronal holes from where the fast wind originates. This imposes basic requirements upon FIP fractionation models, which should reproduce the stronger and more variable low-FIP bias in the slow wind and a weaker (and perhaps conceptually different) low-FIP bias in fast streams. Taken together, these results firmly establish the fundamental difference between the two quasi-stationary solar wind types.

1. Introduction

In April 1998 the Ulysses spacecraft [Wenzel *et al.*, 1992], launched in October 1990, completed the first polar orbit (inclination 80.22°) of a man-made vehicle around the Sun. It has thus mapped the third dimension of the heliosphere, to which access had hitherto been limited owing to the small inclination (7.25°) of the ecliptic plane relative to the heliographic equator. The first set of Ulysses's polar passes took place during the decline to minimum solar activity of cycle 22 and the early onset of cycle 23. At this time the heliosphere was rather simply structured, with large streams of high-speed solar wind at high heliographic latitudes ($\gtrsim 35^\circ$), slow solar wind at low latitudes ($\lesssim 15^\circ$), and these two stream types alternating once per solar rotation at interme-

diate latitudes. That made it quite easy to confirm that the solar wind is a two-state phenomenon, made up of two fundamentally different stream types, as had been found already in the Helios days [Rosenbauer *et al.*, 1977; Schwenn, 1990], and to characterize their properties with unprecedented detail and accuracy.

In this paper we attempt to obtain long-term averages of element and charge state abundances using as many ion species as possible measured on a single instrument, the Solar Wind Ion Composition Spectrometer (SWICS) on Ulysses [Gloeckler *et al.*, 1992], both in the slow and in the fast solar wind. The emphasis is thus on establishing a baseline composition for each solar wind type, rather than studying individual events, spectacular and interesting as they may be. SWICS is a third-generation space mass spectrometer that measures the energy per charge, E/q , time of flight τ , and total energy after postacceleration, E_{tot} , which can be converted to the mass, m , charge, q , and incident energy, E , of the incoming ions, thus fully characterizing them. Between the E/q selection and the τ measurement the ions are accelerated by typically 23 kV, which makes the instrument

¹Department of Atmospheric, Oceanic, and Space Sciences, University of Michigan, Ann Arbor.

²International Space Science Institute, Bern, Switzerland.

³Department of Physics, University of Maryland, College Park.

⁴Max-Planck-Institut für Aeronomie, Katlenburg-Lindau, Germany.

⁵Physikalisches Institut, University of Bern, Bern, Switzerland.

particularly suited for comparative studies between slow and fast solar wind because both types are measured under very similar conditions within the instrument. Furthermore, all ions (except protons and singly charged pickup ions that fall below the energy detector threshold) are generally measured in triple coincidence, thus suppressing the background to extremely low levels. The number of ion species that can be measured by SWICS is limited by its energy and time of flight resolution yet amounts to nearly 40 charge states of 10 elements: H, He, C, N, O, Ne, Mg, Si, S, and Fe.

Charge state and element abundance ratios in the solar wind are important diagnostic tools for at least two reasons: First, the solar wind carries material from the outer convective zone (OCZ) of the Sun into the heliosphere, where it may be analyzed in situ, thus enabling measurements that can be directly compared to remote sensing optical observations of the photosphere and corona. The composition of the OCZ is almost identical to the one of the protosolar nebula and thus establishes the baseline from which our solar system was formed. Notable exceptions are ^2H , which was destroyed, and ^3He , which in turn was enriched in the young Sun [cf. *Geiss and Gloeckler, 1998*]. Second, abundance measurements in the solar wind provide information on the conditions at the site of its origin and on the processes that were active between there and the observing site. Specifically, ratios between charge states can be interpreted as proxies for the coronal electron temperature around 1.5 to 3.5 R_s , called the freezing-in temperature [*Hundhausen, 1972*], and element abundance ratios can be affected by an atom-ion separation process in the upper chromosphere, the first ionization potential (FIP) effect [*Geiss, 1982*]. Charge state and element abundance ratios of heavy ions have been used [*Geiss et al., 1995a; von Steiger, 1998*] to substantiate the relationship between the slow solar wind and the streamer belt [*Feldman et al., 1981*] and to establish that the fast streams emanate from coronal holes, confirming the observations from Skylab [*Krieger et al., 1973*]. Composition measurements, in general, provide the ultimate litmus test to models of solar wind fractionation and/or acceleration, which must contend with observed heavy ion abundances.

1.1. Solar Wind Composition: The Classical Picture

Many space missions and instruments have been flown before Ulysses that already provided quite a coherent picture of the main elemental abundances in the solar wind. It is not the aim of this paper to review these observations, though; see, for example, *von Steiger et al. [1997]* for a fairly recent review.

It has been well established from comparisons of solar wind observations to optical observations in the solar atmosphere (or, for elements that do not have suitable optical transition lines, to local galactic abundances) [*Anders and Grevesse, 1989; Grevesse and Sauval, 1998*] that the slow solar wind composition differs significantly from the photospheric composition. This difference is often displayed in an FIP plot, which gives the FIP factor (or bias), i. e., the double

ratio of the solar wind abundance to the solar abundance of an element X relative to some reference element (usually O), $(X/O)_{\text{SW}}/(X/O)_{\text{Sun}}$, as a function of its FIP. Elements with a low FIP (<10 V, i. e., Mg, Si, and Fe) are enriched by an FIP bias of 3–5 in the slow wind relative to the photosphere [*von Steiger et al., 1997*]. Note, however, that in Figure 9 of *von Steiger et al. [1997]* only the Mg value, which is the lowest one among the low-FIP elements, had been obtained from Ulysses data. Moreover, the preliminary Fe value from SWICS reported by *Ipavich et al. [1992]* is also near the low end of the enrichment factor.

The FIP bias factor is reduced to ~ 1.5 –2 times in the fast streams emanating from coronal holes. On the basis of the smallness of this factor relative to its uncertainty, it became customary to say that the fast streams were hardly fractionated at all and that the fast solar wind may even represent an unbiased sample of solar material from the OCZ. Note, however, that this factor was largely based on measurements of rather short duration in the Earth’s magnetosheath by the charge-energy-mass (CHEM) instrument on Active Magnetospheric Particle Tracer Explorers (AMPTE)/Charge Composition Explorer (CCE) [*Gloeckler et al., 1989*]. Again, only the magnesium value, which is the highest one among the low-FIP elements, had been obtained from Ulysses by *von Steiger et al. [1997]*.

The transition from low- to high-FIP elements is near ~ 10 V, and the elements near this value, S and C, are partially enriched, whereas the true high-FIP elements, O, N, Ar, and Ne (FIP >10 V), are not enriched and not fractionated relative to each other. The status of H, which coincidentally has the same FIP as O, is difficult to establish, but it seems that it behaves largely as the other high-FIP elements do or may be somewhat enriched above them (or rather the other way round, if we take H to represent the baseline).

Helium, the element with the highest FIP, is a special case because it is ~ 2 times depleted relative to the other high-FIP elements, both in the slow wind and in fast streams. This is probably not the result of a FIP fractionation effect alone, as helium has the least favorable Coulomb drag factor for acceleration by friction with protons, which may lead to an additional depletion in the slow wind [*Geiss, 1982*].

Time-averaged solar wind abundances of the heavy noble gases, Kr and Xe, can be obtained from inclusions in the lunar regolith [*Wieler, 1998*]. They do not readily fit into the FIP pattern outlined above but appear to be enriched above the high-FIP elements even though their FIP is high as well. It has been argued that the first ionization time (FIT) seems to be a better organizing parameter [*Geiss et al., 1994a*], motivated by the fact that the element fractionation can be pictured as the result of a competition between photoionization and dynamic atom-ion separation. However, we prefer to retain FIP as the main organizing parameter since it is a fundamental atomic property, whereas the FIT is a convolution of the ionization cross section with the solar EUV spectrum, which is very variable over the solar activity cycle.

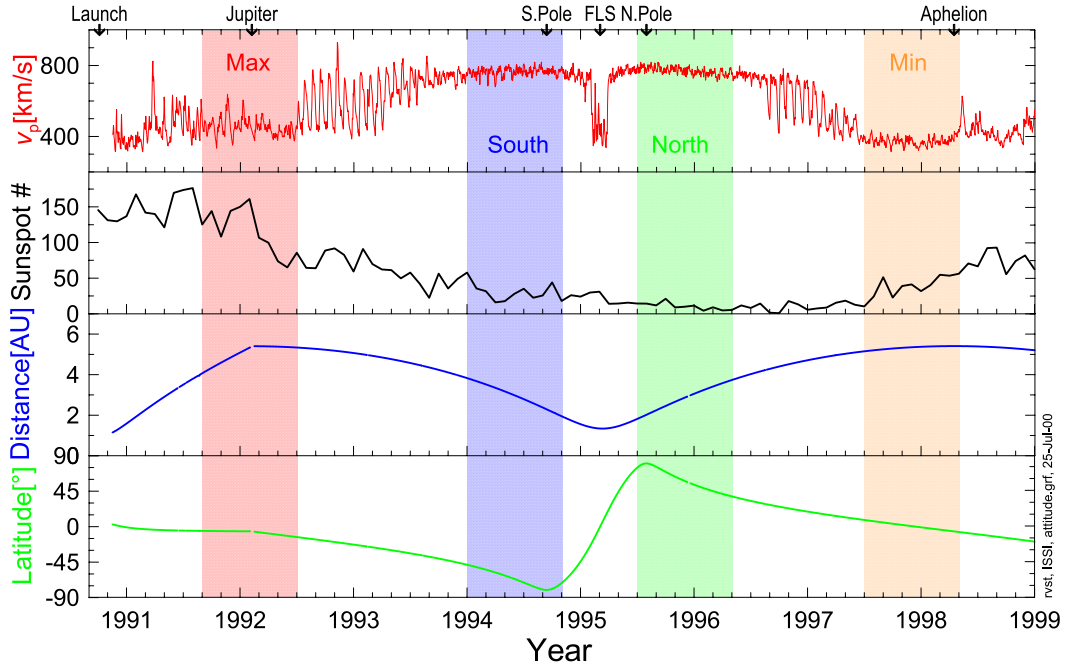


Plate 1. Data periods selected for this study (shaded bands) in relation to heliospheric and Ulysses attitude parameters: solar wind speed of protons from the Solar Wind Observations Over the Poles of the Sun (SWOOPS) sensor [Bame *et al.*, 1992], v_p ; sunspot number; Ulysses heliocentric distance; and heliographic latitude (top to bottom panels). Two periods sample slow solar wind (red and orange), one after solar maximum of cycle 22 and the other during a remarkably quiet time at the onset of cycle 23; and another two periods sample fast solar wind from the polar coronal holes around the minimum of cycle 22 (blue and green).

2. SWICS Data Selection and Analysis

2.1. Selection of Time Periods

For the analysis reported here we need long time periods when Ulysses was immersed in either solar wind type and that were largely unperturbed by strong transient or recurrent events such as coronal mass ejections (CMEs) or corotating interaction regions (CIRs). Over the mission duration of more than 8 years (and counting) and the completion of a full high-inclination orbit, we have selected the following four ~ 300 -day periods of Ulysses/SWICS data for this study (see also Plate 1): (1) September 1991 to June 1992 (Day of year (DOY) 244-1991 to 182-1992, excluding 10 days around Jupiter encounter), low latitudes, relatively quiet, and slow solar wind at postmaximum solar activity (period “Max,” red); (2) January – October 1994 (DOY 001-1994 to 304-1994), high latitudes and fast stream from South Polar coronal hole (period “South,” blue); (3) July 1995 to April 1996 (DOY 182-1995 to 121-1996), high latitudes and fast stream from North Polar coronal hole (period “North,” green); (4) July 1997 to April 1998 (DOY 182-1997 to 120-1998), low latitudes, quiet, and slow solar wind at postminimum solar activity (period “Min,” orange). These periods are considered as representative for the state of the solar wind around the activity minimum between cycles 22 and 23. During the first period (“Max”), solar activity was still quite high, and the solar wind speed consequently

was quite variable, owing to the occurrence of CMEs and even some small fast streams from equatorial (extensions of) coronal holes. Nevertheless, the majority of these CMEs have a composition very similar to the surrounding slow solar wind [Neukomm, 1998], and the fast streams (or rather, streamlets) were too few as to significantly affect the abundance determination. As will be seen in section 3.2, the results from this period are statistically indistinguishable from those obtained during the fourth period (“Min”), which is an exceptionally long and quiet period of slow solar wind with virtually no interference from CMEs or fast streams: it is perhaps the most pristine sample of purely slow solar wind in our survey. Our choice of these two periods of slow wind was not motivated by speed alone but strongly influenced by composition signatures as well. As will be shown in section 3.4, the charge state composition of heavy ions is perhaps the most powerful feature to tell slow wind from fast streams. No attempt can nor should be made to interpret the results from these two periods as solar maximum versus solar minimum. For such a comparison to be made with confidence one has to await at least the next set of polar passes of Ulysses in 2000–2001. The two middle periods (“South” and “North”) are obviously representative of the fast streams from the polar coronal holes. Even so, at least the “South” period is very slightly contaminated by a small number of CMEs [Gosling *et al.*, 1995], but all of them have been shown to have a composition that is indistinguish-

able from the surrounding fast wind [Neukomm, 1998], so the contamination is of even less concern in this case.

One might argue that the two slow periods (“Max” and “Min”) and the two fast periods (“South” and “North”) were obtained at systematically different spacecraft attitudes.

Both slow samples are from large distances (> 4 AU) and low latitudes ($< 10^\circ$), while both fast samples are from intermediate distances (2–4 AU) and high latitudes ($> 40^\circ$). This is an inevitable consequence of the combination of Ulysses’s high-inclination orbit and the simple structure of the minimum heliosphere. However, we do not believe that this fact will affect the comparison of the slow to the fast samples because, as discussed in the previous paragraph, the specific, characteristically different properties of the fast streams as compared to the slow wind were also found before Ulysses at Earth orbit [e. g., von Steiger et al., 1992].

2.2. Data Analysis Procedure

The results reported in this work were exclusively obtained from the pulse height analysis (PHA) words of Ulysses/SWICS [Gloeckler et al., 1992]. This data type contains the full time of flight τ and total energy ε information of a selected number of ions, which in principle, together with the energy per charge, E/q , setting of the entry system, uniquely identifies the ion species. The number of PHA words is limited by telemetry to 8 or 30 per spacecraft spin, but this limitation is not severe under most circumstances. The solar wind flux of heavy ions (i. e., carbon and heavier elements) is generally low enough so that the necessary correction factors can be determined very accurately from the basic rates that are also provided by the sensor.

The PHA counts are then analyzed using a newly developed procedure and improved analysis techniques that are described in full detail in Appendix A. We nevertheless find it useful to summarize the procedure here by giving a brief outline of the steps involved. It is based on earlier work by Wimmer-Schweingruber [1994] and von Steiger [1995], but it standardizes those procedures, adds important steps, and revises others to make them more reliable.

In a first step each PHA event is assigned to an ion species if it falls within one standard deviation from any one ion peak in the (τ, ε) matrix (cf. Plate A2). The positions and widths of these ion peaks as a function of E/q (the “forward model”) were originally determined by Wimmer-Schweingruber [1994] but have now been extensively revised and newly parameterized using the massive amount of in-flight data that have become available in the meantime. PHA events falling outside a $1\text{-}\sigma$ region around any one ion peak remain temporarily unused until the fourth analysis step described below.

In a second step, the ion count rates so obtained are corrected for a priorization scheme of the instrument, which is needed to telemeter as many of the heavy ($A \geq 12$) ion events as possible that are far less abundant than H and He.

The corresponding correction factors normally are not much larger than 1 and less than ~ 2 under most conditions, which means that the statistical sample of selected PHA words accounts for at least 50% of the population, making it very unlikely to be biased in any way.

In a third step these count rates are corrected for mutual spillover of one ion peak into the $1\text{-}\sigma$ region around another by using a linear inversion procedure. As this may result in negative count rates for some ion species, these species are temporarily removed from further consideration, using a correction procedure that avoids any bias to the other, positive species. Such an ion species can be considered as too rare to produce a significant count rate, which may occur in the neighborhood of another, more abundant species.

The fourth step then is to assign a unique identity to each PHA word according to a new, probabilistic scheme. At this step all PHA words are again considered, so the full count statistics is exploited. The probability of a count to be assigned to a specific ion species is proportional to the value of that ion peak at its position in (τ, ε) space. The assignment is done using a random number, which means that different analysis runs of the same time period do not produce exactly equal results. However, these differences by design remain within the Poissonian statistical error estimate, which is verified by executing this analysis step two or three times in a row.

As mentioned in section 1 no background corrections had to be made to the count rates so obtained, with the exception of the lowest charge states of Fe ($q \leq 8$), where accidental time of flight coincidence counts were removed. Such spurious counts are triggered by two different protons, one generating a start signal but not a stop signal, which is then generated by a second proton later. Strictly speaking, this is not really a background correction: Although accidental coincidence counts can be classified as low-charge Fe ions by the forward model, they occur at different, much lower E/q values than the real Fe counts do, so they can be cut out in the E/q spectra without affecting the real Fe counts and their statistical uncertainty.

We now have the count rates of each ion species as a function of energy per charge, $C_i(E/q)$, which are then transformed into differential flux $dj_i(E/q)$ according to

$$dj_i(E/q) = \frac{C_i(E/q)}{t_{\text{acc}} g \eta_i(E/q, \alpha)}, \quad (1)$$

where t_{acc} is the accumulation time, g is the sensor’s geometry factor, and $\eta_i(E/q, \alpha)$ is the detector efficiency. The latter is also a weak function of the Sun aspect angle α , which implies that t_{acc} should be limited to time periods over which α does not vary strongly, which is usually the case for several weeks or even months.

Differential flux is then conveniently transformed to phase space density to obtain the distribution function

$$f_i(E/q) = \frac{1}{2\delta} \left(\frac{m/q}{E/q} \right)^2 dj_i(E/q), \quad (2)$$

where $\delta = \Delta(E/q)/(E/q)$ is the electrostatic analyzer constant. Note that the exact factor 1/2 applies when all quantities are expressed in SI units but is replaced by 0.537 when expressing E/q in keV e^{-1} , m/q in amu e^{-1} , and dj in $\text{cm}^{-2} \text{s}^{-1}$. Finally, density, velocity, and thermal speed of each species can be obtained by taking the appropriate moments of the velocity distribution function derived from (2).

2.3. Estimates of Systematic Error

There are essentially two sources of systematic uncertainty associated with the measured quantities.

2.3.1. Ion identification. The widths of the ion peaks in the (τ, ε) matrix are of the order of 1.5% in the τ direction and 10% in the ε direction. Neighboring ions therefore may overlap, and imperfections in the forward model may lead to systematic errors in the probabilistic identity assignments. The most obvious victims of this effect are all charge states of N, situated between more abundant charge states of C and O, and Mg^{9+} , situated just above the most abundant of the heavy ions, O^{6+} . Also, the Mg, Si, and S ion peaks overlap considerably, which may lead to some misidentifications of such ions. We note, however, that the abundance ratio of low- to high-FIP elements, $(\text{Mg}+\text{Si}+\text{S}+\text{Fe})/(\text{C}+\text{N}+\text{O}+\text{Ne})$, will be quite unaffected by this effect, as the main confusions are limited to within these two ion groups rather than between them.

2.3.2. Detector efficiencies. A model for the efficiencies has been developed by *von Steiger* [1995] and tuned to best fit the data of the extensive preflight calibrations. However, there are two drawbacks to this approach: Owing to limitations even of one of the best calibration facilities available in 1990, the calibration system for mass spectrometers (CASYMS) at the University of Bern [*Ghielmetti et al.*, 1983; *Steinacher et al.*, 1995], most ion species were only available with relatively few charges, and no ion beams could be obtained of refractory elements such as Si and Fe. The efficiency model therefore had to be extrapolated to ions with higher charges and interpolated between ion species, leading to some uncertainty. However, the maximum possible systematic error is limited to a few tens of percent at worst even without any model because all heavy ($A \geq 12$) ion efficiencies are $\gtrsim 50\%$ at energies typical for the solar wind and by design cannot exceed 100%.

In summary, the total systematic measurement errors in the abundance values reported in section 3.2 are estimated to be better than 10% for C and O, better than 20% for most of the other elements, and better than 30% for the elements that are most difficult to identify, N and Ne. The statistical uncertainty can always be reduced below the systematic one simply by accumulating data over a sufficiently long time period. Typical count rates near aphelion (~ 5 AU) are of the order of 1000 per day for oxygen and 100 per day for iron, and typical count rates are correspondingly higher over the poles (8 times) and near perihelion (16 times). Therefore an accumulation over one day is usually sufficient for the determination of element ratios, but for the less abundant

individual charge states an accumulation over several days may be needed.

3. Results

3.1. Overview

Using the new analysis techniques described in section 2.2 and detailed in Appendix A, we have reanalyzed the complete Ulysses/SWICS data from launch to the end of 1998. The data coverage of Ulysses is extremely good, 96% or higher, with only nine data gaps of a few days duration each during the whole mission so far. (The data gaps are, in fact, much shorter than that, but SWICS needs a few days for its high voltage to be ramped up to the operational value.)

As a basis for further analysis, we have obtained velocity distribution functions of 37 different ion charge states (He^{2+} , C^{4-6+} , N^{5-6+} , O^{6-8+} , Ne^{8+} , Mg^{6-10+} , Si^{7-12+} , S^{8-11+} , and Fe^{6-16+} , in triple coincidence, plus H^+ and once again He^{2+} in double coincidence) at time resolutions of 1, 5, 25, and 125 days. From the distribution functions we calculate density, bulk speed, and thermal speed of each ion species to obtain time series of these quantities. (Of course, the bulk speeds and particularly the thermal speeds determined from the longer-term accumulations are not very relevant as they are likely to be dominated by true speed variations during the accumulation period rather than the thermal motion.)

An overview of a few selected parameters so obtained is given in Plates 2 and 3. The bulk speed of protons, v_p from Solar Wind Observations Over the Poles of the Sun (SWOOPS), is repeated from Plate 1 in the top panels of Plates 2 and 3 for facilitating the orientation. In earlier work we have often used the speed of alpha particles, v_α , determined with SWICS in this context. This has the advantage that all data are from the same instrument but the disadvantage that v_α does not strictly represent the bulk speed of the solar wind. The E/q analyzer of the SWICS main channel cuts off protons below 350 km s^{-1} , making it difficult or impossible to reliably determine v_p with this sensor if the speed gets near or even below this threshold. We therefore now use v_p from SWOOPS, and in order to relate this work to earlier publications we have compared that speed to v_α from SWICS at a time resolution of 1 day (i. e., almost 3000 samples). We find a very tight relationship of

$$v_{\alpha, \text{SWICS}} = 1.004 v_{p, \text{SWOOPS}}, \quad (3)$$

with a correlation coefficient of $r^2 = 0.9995$, that is, the two speeds agree to better than 0.5%. If restricted to the polar fast streams in 1994 to mid-1996 we even find that the speed of the alpha particles, which are accelerated by outward travelling Alfvén waves, exceeds the proton speed by $\sim 1.2\%$ or 10 km s^{-1} , as expected (see Figure 1).

From the density ratios plotted in Plate 2, two observations can readily be made: First, abundances of low-FIP elements such as Si and Fe are enhanced relative to O in the slow solar wind (the well-known FIP effect), and second, all

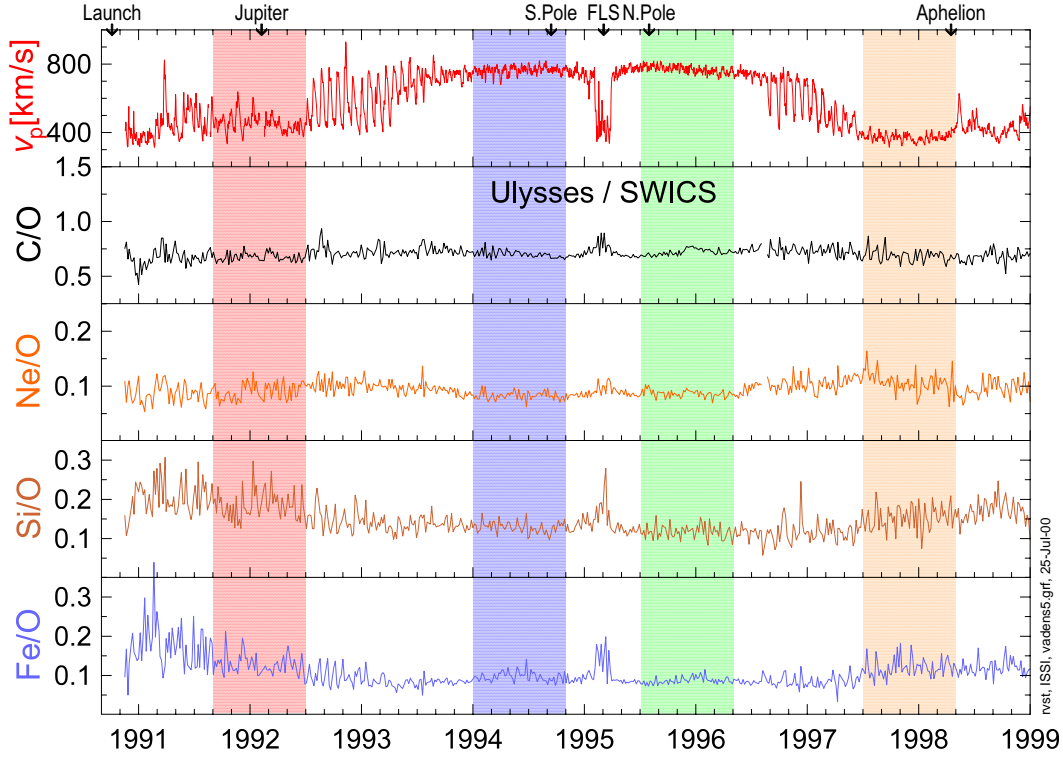


Plate 2. The 5-day average values of the abundance ratios C/O, Ne/O, Si/O, and Fe/O (second to fifth panels) in comparison to the solar wind speed of protons repeated from Plate 1 (first panel). The enhanced abundance of Si and Fe (i. e., low first ionization potential (FIP) elements) in the slow solar wind becomes readily apparent in this representation, whereas no such effect may be seen in C and Ne (i. e., high-FIP elements).

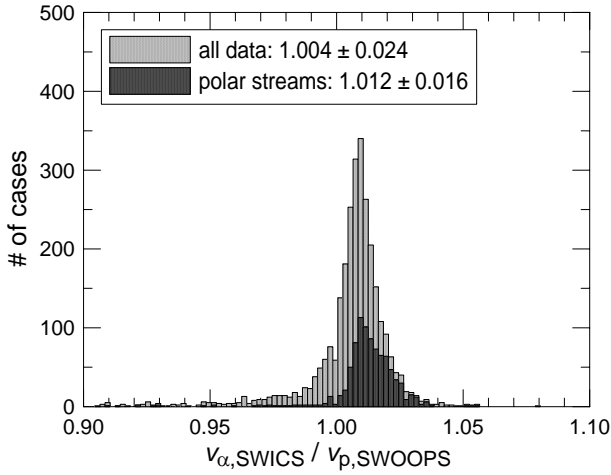


Figure 1. Daily values of the speed of alpha particles as measured on Ulysses by Solar Wind Ion Composition Spectrometer (SWICS) relative to the speed of protons as measured by SWOOPS. On average, the two speeds agree to better than 0.5% (light histogram); if restricted to the polar fast streams the alpha particles outrun the protons by $\sim 1.2\%$ or 10 km s^{-1} .

abundance ratios are more variable in the slow solar wind, as is more clearly visible in the low-FIP elements, but may also be seen in the high-FIP ones.

The difference between slow solar wind and fast streams is even better discernible in some of the freezing-in temperatures given in Plate 3. These temperatures are obtained in the usual way by converting the indicated charge state ratio to the temperature that would be needed to establish that ratio under collisional equilibrium with ambient electrons. The conversions are done using the tables of *Arnaud and Raymond* [1992] for Fe and *Arnaud and Rothenflug* [1985] for all other elements. Freezing-in temperatures are proxies for the coronal electron temperature near the altitude where the expansion timescale of the accelerating solar wind increases above the ionization/recombination timescales. This altitude is typically in the range $1.2\text{--}3.5 R_s$, depending on the pair of charge states considered. The values obtained from several charge state ratios may even be used to derive a rough temperature profile of the corona [*Geiss et al.*, 1995b; *Ko et al.*, 1997]. The time series of freezing-in temperatures given in Plate 3 qualitatively show a rather similar picture as those of the abundance ratios above: Firstly, some of the ratios are strongly anticorrelated with the solar wind speed, cooler in the fast streams than in the slow wind, while others hardly show any such systematic variation. However, the division is not simply between high- and low-FIP elements as it may

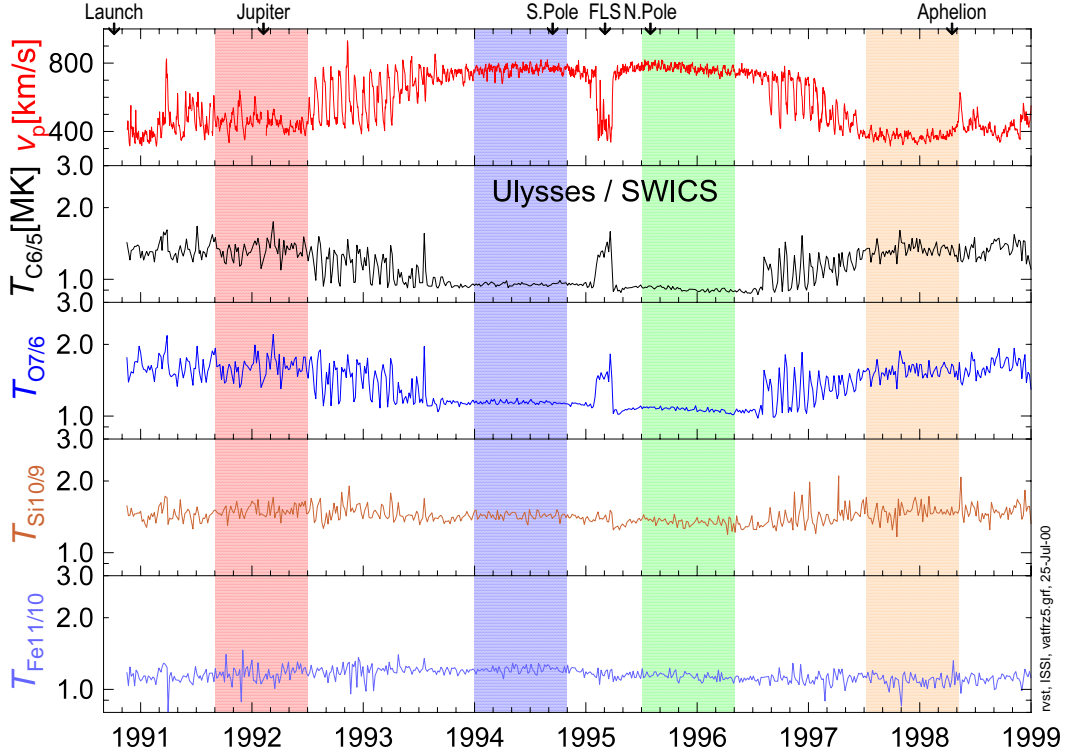


Plate 3. The 5-day average values of selected charge state ratios, converted to freezing-in temperatures: $T(C^{6+}/C^{5+})$, $T(O^{7+}/O^{6+})$, $T(Si^{10+}/Si^{9+})$, and $T(Fe^{11+}/Fe^{10+})$ (second to fifth panels) in comparison to the solar wind speed of protons repeated from Plate 1 (first panel). A strong anticorrelation of the C and O temperatures to v_p may easily be seen, whereas no such effect is apparent in the Si and Fe temperatures.

seem. Ratios of the higher charge states of Si and Fe are also strongly dependent on the solar wind type. We will return to this point further in section 3.3. Secondly, just like in the case of the abundance ratios, the variations of the charge state ratios are also much more variable in the slow solar wind than in fast streams.

Taken together, Plates 2 and 3 confirm the picture of the solar wind as a two-state phenomenon around the minimum phase of the solar activity cycle, with slow solar wind of variable composition prevalent at low latitudes, and high-speed streams of much more uniform composition dominating the high-latitude heliosphere. We now turn to the mean properties of these two wind types.

3.2. Average Solar Wind Elemental Composition

In Table 1 and Plate 4 we summarize the element abundances obtained during the four ~ 300 -day periods defined in Plate 1. The tabulated numbers indicate averages of the daily values relative to O, and the $1-\sigma$ error bars of the samples are also given. These do not denote the uncertainty of the averages (which would be smaller by a factor of about $\sqrt{300}$ because there are some 300 samples in the average) but are indicators of the natural variability of the daily values. As expected from Plate 2, this variability is much smaller in the fast streams than in the slow wind.

The first point to note in Plate 4 is that there is no systematic difference between the two samples in the slow wind (i.e., the compositions in the “Max” and in the “Min” periods are the same) nor between the two samples in the fast streams (i.e., the composition in the “South” and the “North” polar coronal hole associated wind is identical). It is therefore justified to consider the sums of the “Max” and the “Min” periods as representative for the slow wind and of the “South” and the “North” period as representative of the fast wind, as we have done in Table 2.

Next, we observe that neon in the fast streams and both nitrogen and neon in the slow wind appear to be depleted relative to O, i.e., to an FIP bias of < 1 . We recall that these high-FIP elements are most difficult to identify in the (τ, ε) matrix, and the depletion might thus be an artifact of systematic error. The large variability of the ~ 300 daily values of N in the slow wind, which considerably exceeds the statistical uncertainty of a typical daily value, in our view supports this interpretation. The low Ne value is more difficult to interpret, even though it agrees quite well with an earlier determination by *Geiss et al.* [1994b]. One may thus be tempted to claim that Ne, just like He (discussed in section 1), is truly depleted in the solar wind. However, this would be at variance with earlier results obtained with the foil collection technique [*Geiss et al.*, 1972] and confirmed by *Bochsler et al.* [1986]. We therefore cannot rule out that

Table 1. Abundance Ratios Relative to Oxygen Obtained With Ulysses/SWICS During the Four ~ 300 -Day Periods Defined in Plate 1^a

	FIP	“Max”	“South”	“North”	“Min”	Phot.
He	24.59	95.9 \pm 35.1	72.7 \pm 7.9	73.6 \pm 8.2	84.0 \pm 33.0	126
C	11.26	0.670 \pm 0.071	0.683 \pm 0.040	0.703 \pm 0.037	0.670 \pm 0.086	0.489
N	14.53	0.069 \pm 0.038	0.111 \pm 0.022	0.116 \pm 0.021	0.088 \pm 0.035	0.123
O	13.62	$\equiv 1 \pm 0$	$\equiv 1 \pm 0$	$\equiv 1 \pm 0$	$\equiv 1 \pm 0$	$\equiv 1$
Ne	21.56	0.091 \pm 0.025	0.082 \pm 0.013	0.084 \pm 0.013	0.104 \pm 0.027	0.178
Mg	7.65	0.147 \pm 0.045	0.105 \pm 0.025	0.108 \pm 0.022	0.143 \pm 0.055	0.0560
Si	8.15	0.167 \pm 0.047	0.115 \pm 0.023	0.102 \pm 0.023	0.132 \pm 0.042	0.0525
S	10.36	0.049 \pm 0.016	0.056 \pm 0.013	0.051 \pm 0.014	0.051 \pm 0.021	0.0316
Fe	7.87	0.120 \pm 0.039	0.092 \pm 0.017	0.081 \pm 0.014	0.106 \pm 0.044	0.0468

^aThe numbers denote averages of daily values with their 1- σ variability. Photospheric (Phot.) values are from *Grevesse and Sauval* [1998]. SWICS, Solar Wind Ion Composition Spectrometer; FIP, first ionization potential.

Ne might still be significantly affected by systematic error and that the true value may perhaps be 30% higher.

Most importantly, we observe that the enrichment factors of the low-FIP elements look different from the classical picture described above. The FIP bias appears to be smaller than the canonical factor of 3–5 in the slow wind [von Steiger et al., 1997] but the FIP bias is clearly larger than 1 in the fast streams. Depending on how we define the FIP enhancement factor in the solar wind (SW) relative to the photosphere (Ph),

$$f = \frac{\left(\frac{[\text{Mg}]+[\text{Si}]+[\text{S}]+[\text{Fe}]}{[\text{C}]+[\text{N}]+[\text{O}]+[\text{Ne}]} \right)_{\text{SW}}}{\left(\frac{[\text{Mg}]+[\text{Si}]+[\text{S}]+[\text{Fe}]}{[\text{C}]+[\text{N}]+[\text{O}]+[\text{Ne}]} \right)_{\text{Ph}}} \quad (4)$$

or

$$f_{\text{O}} = \frac{\left(\frac{[\text{Mg}]+[\text{Si}]+[\text{Fe}]}{[\text{O}]} \right)_{\text{SW}}}{\left(\frac{[\text{Mg}]+[\text{Si}]+[\text{Fe}]}{[\text{O}]} \right)_{\text{Ph}}}, \quad (5)$$

we obtain the values collected in Table 2 (square brackets around element symbols denote elemental abundances). The lower values of the FIP bias factors are partially due to recently revised photospheric abundances. In particular, the photospheric oxygen abundance was decreased by 0.1 decades ($\sim 20\%$) by *Grevesse and Sauval* [1998] as compared to that by *Anders and Grevesse* [1989], which directly translates into a corresponding decrease of f and f_{O} . Fractionation factors based on the older photospheric composition (used by von Steiger et al. [1997]) are given in parentheses in Table 2 and are generally higher; it is this value of f_{O} that should be used in comparisons to fractionation factors published earlier.

Whatever the adopted composition of the photosphere, it is evident from Plate 4 and Table 2 that the difference in FIP

Table 2. FIP Enhancement Factors of Low-FIP Elements in Slow and Fast Solar Wind, Referred to the Sum of the High-FIP Elements, f , or to Oxygen Alone, f_{O} , Based on the Photospheric Abundances of *Grevesse and Sauval* [1998]^a

	“Max”+“Min”	“South”+“North”
f	2.4 (3.0)	1.8 (2.3)
f_{O}	2.6 (2.9)	1.9 (2.1)

^aValues referred to an older compilation of the photospheric composition [Anders and Grevesse, 1989] are given in parentheses.

bias between the two solar wind types is not as strong as was previously thought. However, the fractionation factors reported here are not truly at variance with previous results: It only seems that the FIP bias factor derived in this work (2.9 or 3.0 if referred to the older photospheric abundances) is close to the low end of the values in the slow wind reported earlier (3–5 [von Steiger et al., 1997]), whereas it is near the high end in fast streams. We should like to stress again that the slow wind to fast wind comparison can be made quite reliably with the new analysis techniques used here. The reason for this confidence stems mainly from the probabilistic identity assignment of individual pulse height analysis (PHA) events. This step ensures some independence from possible imperfections in the positions and, in particular, the widths of the ion peaks provided by the forward model. An uncertainty in the peak width was transferred directly to the corresponding ion count rate in the old scheme, whereas the

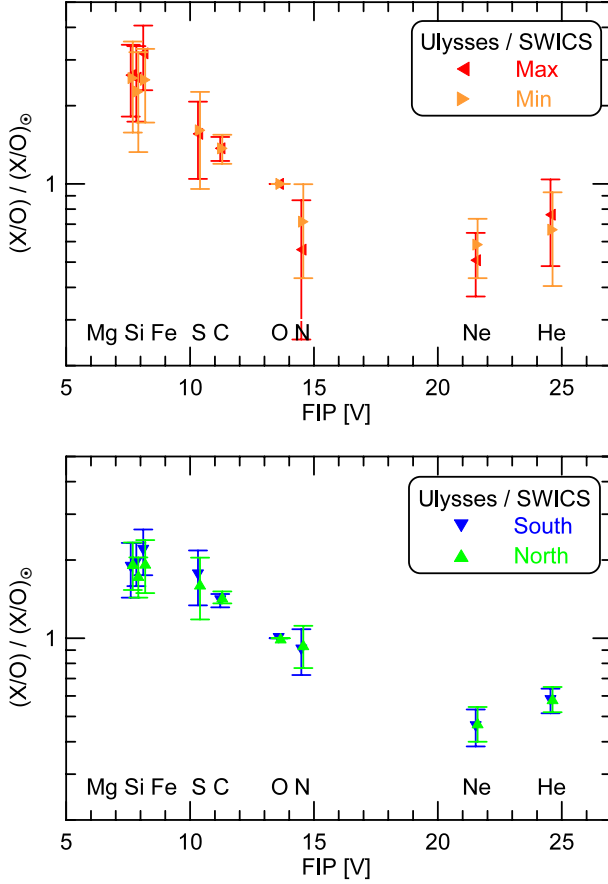


Plate 4. Average element abundance ratios relative to oxygen from Ulysses/SWICS during (top) two ~ 300 -day periods of slow solar wind and (bottom) two periods of fast streams. The ratios are divided by the solar surface ratio and plotted as a function of the first ionization potential (FIP). The data points indicate the averages of the daily values, and the error bars span the $1\text{-}\sigma$ range of their variability. Evidently the two samples of each individual wind type agree very well among each other, but the enhancement of low-FIP elements, while clearly present in the fast streams, is stronger in the slow solar wind.

probabilistic assignment is less directly dependent on these parameters, at least for large and for isolated peaks.

3.3. Average Solar Wind Charge State Distributions

In Plate 5 we report the average charge state spectra (density of individual charge states relative to element density) of C, O, Si, and Fe, again obtained during the four ~ 300 -day periods defined in Plate 1. There are large differences of the spectra from the different solar wind types, but although the two spectra from the same solar wind type look very much alike, there are small but statistically significant differences between them as well.

The obvious point noted first in Plate 5 is a general shift toward higher charge states in the slow wind as compared to fast streams. Considering Plate 3, this comes as no surprise

Table 3. Freezing-in Temperatures of C, O, Si, and Fe, Observed in the Fast Streams From the South and the North Polar Coronal Holes and in the Slow Solar Wind^a

	“Max”	“South”	“North”	“Min”
T_C , MK	1.37	0.98	0.93	1.34
T_O , MK	1.64	1.12	1.05	1.52
$T_{Si,bulk}$, MK	1.62	1.41	1.35	1.55
$T_{Si,max}$, MK	1.66			1.59
$T_{Fe,bulk}$, MK	1.14	1.26	1.20	1.10
$T_{Fe,max}$, MK	3.0			2.0

^aWhereas the samples from fast streams can be quite well represented by a single freezing-in temperature for each element, no single temperature can be defined for Si and Fe in the slow solar wind. We therefore list two values in those columns, one for the lower charge states (Si^{7+} – Si^{10+} and Fe^{6+} – Fe^{13+} , respectively), T_{bulk} , and another corresponding to the highest observed charge state (Si^{12+} and Fe^{16+} , respectively), T_{max} . Columns “South” and “North” are for the observations in the fast streams from the South and the North Polar coronal holes. Columns “Max” and “Min” are for observations in the slow solar wind, as indicated in Plate 1.

in the case of C and O (top panels in Plate 5), since that shift translates directly into a higher freezing-in temperature. The situation for the elements that are spread over many charge states is less simple, though. It seems that the distributions of Si and Fe (bottom panels in Plate 5) are quite similar at the lower charge states in all four samples, but there is a substantial excess of high charge states in the slow wind samples. Such an excess was in fact predicted by *Bürge* [1987] for Si in his “hot” model (i. e., the one without a suprathermal tail on the electron distribution function) and first observed by *Galvin et al.* [1992] for Si and by *von Steiger et al.* [1997] for Fe. We will return to this point below.

The samples from fast streams (“South” and “North”) can be quite well represented by a single freezing-in temperature for each element, listed in Table 3, a fact already noted by *Geiss et al.* [1995b]. This could be interpreted as the freezing-in process occurring rather rapidly in the freely expanding fast solar wind, combined with the fact that the recombination rates of the relevant charge states of each element are rather similar, so they all freeze-in at much the same altitude, or temperature, in the corona. From Table 3 we note that the North Polar coronal hole was some 60,000 K cooler than the one in the south, confirming a finding of *Galvin et al.* [1997]. We think the difference is largely a spatial effect, as the temporal trends appear to be too small to account for its magnitude: In the fast stream from the south hole the oxygen freezing-in temperature drops at an average linear rate of $dT_O/dt = -16,000 \text{ K yr}^{-1}$, and in the north hole at $dT_O/dt = -26,000 \text{ K yr}^{-1}$ (compare the third panel

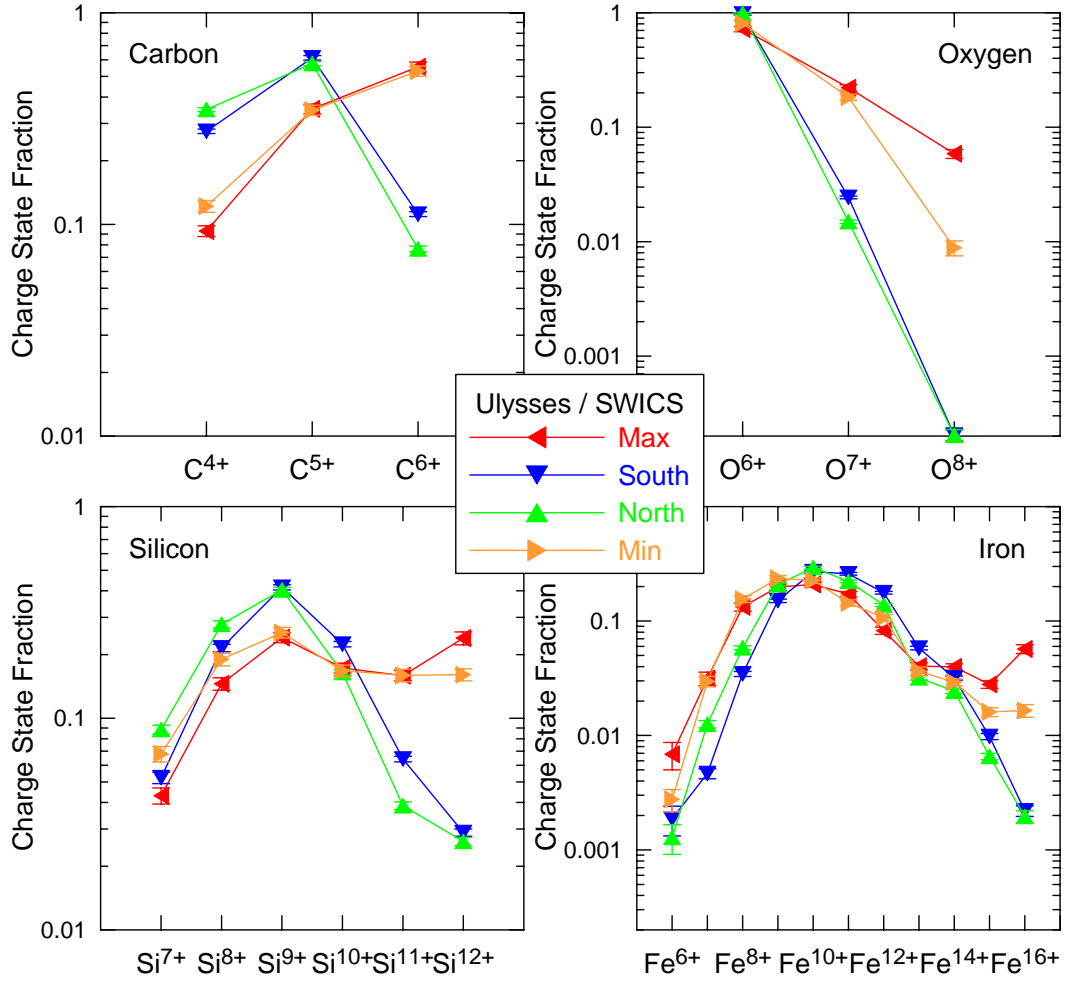


Plate 5. Average charge state spectra of C, O, Si, and Fe from Ulysses/SWICS, obtained during the four ~ 300 -day periods defined in Plate 1. As in Plate 4, data points denote averages of the daily values, but here the bars indicate the errors of the mean values.

in Plate 3), whereas the drop during the fast latitude scan from south to north (defined as the mismatch between the two trend lines) was a full $-43,000$ K in just 3 months, some 8 times larger than the average trend within the holes. However, since the observations in the north and south coronal holes were not taken simultaneously, it is not strictly possible to rule out a temporal effect for part of or even the whole temperature difference.

In Table 3 we also list the freezing-in temperatures observed in the slow solar wind. As mentioned above, no single temperature value can describe the spectra of the elements that are distributed over many charge states. For these elements (Si and Fe) we thus give two values, one corresponding to the bulk of lower charge states and another corresponding to the highest charge state observed. The difference between these temperatures is insignificant for Si but substantial for Fe. It is interesting to note that $T_{\text{Fe,bulk}}$ is some $100,000$ K lower in the slow wind than it is in fast streams (columns “South” and “North”), although the C and O temperatures are significantly higher there (com-

pare Plate 3). The higher temperature of the corona in the streamer belt as compared to the coronal holes apparently does not cause the charge state distribution of Fe to uniformly shift to higher charge states, as might be expected if we were to interpret the freezing-in process in the same way as in coronal holes. Rather, the charge state distribution remains very similar or even shifts somewhat to lower charge states, but high charge states (Fe^{14+} – Fe^{16+}) are added on top of it. This indicates that the slow wind plasma has undergone a more complicated thermal history than the fast streams, or rather that it may be composed of contributions with a range of different temperatures. The situation may be understood in the context of a new magnetic field model [Fisk et al., 1999b] if these contributions are identified with stemming from previously closed loops of different ages, sizes, and temperatures that are opened up by the field lines migrating along the coronal streamer belt. This view is also supported by the observations of Aellig et al. [1998], which have shown that the iron charge states vary rapidly, on timescales that are consistent with those expected from the Fisk field model. We will discuss these points further in section 3.4.

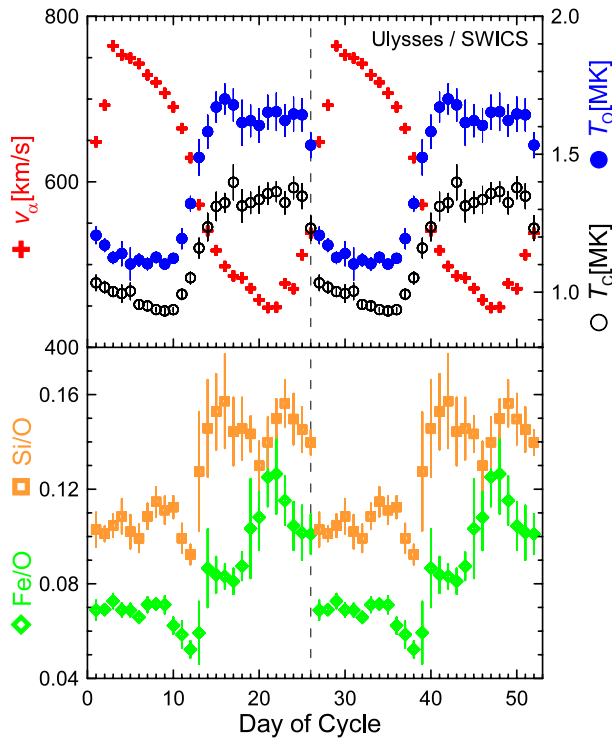


Plate 6. Superposed epoch plot of alternating slow solar wind and fast streams in 1992–1993 [after *Geiss et al., 1995b*]. Nine recurrences of an average duration of 26 days were superposed, and the resulting time series is repeated twice to emphasize the periodicity. It is evident that the speed profile is strongly anticorrelated to the freezing-in temperatures (top panel), which in turn are well correlated with the compositional signatures (bottom panel).

3.4. Synopsis of Alternating Stream Types

As a last item, mainly to stress again that the new analysis methods do not substantially alter previous results, we repeat the superposed epoch analysis of *Geiss et al. [1995b]* of the period with alternating stream types in 1992–1993. (We have not extended the analysis to the similar period in 1997–1998, though, since the heliospheric current sheet was much flatter during that time, thus making the transitions between the stream types less well defined; see *Wimmer-Schweingruber et al. [1999]* for an account of that period.) The result of the superposition is given in Plate 6, which agrees very well with Figure 3 of *Geiss et al. [1995b]*, except that we have added Si/O in place of Mg/O so between their figure and ours all three low-FIP elements are represented. Plate 6 summarizes in a compact manner the most essential result of SWICS regarding solar wind composition, namely, that there are two types of solar wind that not only differ in speed (a heliospheric signature) but also differ in their charge state composition (a coronal signature) and even in their elemental composition (a chromospheric signature). Taken together, this reiterates that the solar wind is a two-state phenomenon, with a sharp boundary separating the two states in the helio-

sphere, through the corona, and all the way down into the chromosphere.

4. Discussion

The abundance observations of Ulysses/SWICS provide detailed requirements for theories of elemental fractionation in the solar wind and for solar wind acceleration theories. These requirements can be summarized as follows:

1. There exists a bias of low-FIP elements relative to photospheric abundances in both the fast and slow solar wind.
2. The low-FIP bias in the slow solar wind is stronger by about a factor of 2 than in the fast solar.
3. The variability of elemental abundances is stronger in the slow solar wind than in the fast solar wind. For example, the $1-\sigma$ variability for Fe in the slow solar wind exceeds 40% for the period closest to solar minimum (“Min”) while it is less than 20% in fast solar wind streams (compare Table 1).
4. The charge state distributions for all species are very different in fast and slow solar wind. For carbon and oxygen, charge states in fast and slow solar wind may be used to easily characterize a freezing-in temperature, formed at the point when the solar wind convection time becomes smaller than the ionization and recombination times. The oxygen freezing-in temperature is ~ 1.1 MK in the fast solar wind and about ~ 1.6 MK in the slow solar wind.
5. The charge states of elements heavier than oxygen and carbon cannot be easily characterized by a single freezing-in temperature in slow solar wind.

Taken together, these observations show that the sources and elemental fractionation processes are fundamentally different in fast and slow solar wind. The charge states also constrain acceleration models of the solar wind [*Ko et al., 1997*]. Indeed, models of elemental fraction and models of solar wind acceleration must contend with these observations.

There are many theories for the acceleration of solar wind [e.g., *Hundhausen, 1973; Hollweg, 1978; Bürgi and Geiss, 1986; McKenzie et al., 1995; Fisk et al., 1999a*] and for the formation of FIP biases in the solar wind [e.g., *von Steiger and Geiss, 1989; Ip and Axford, 1991; Marsch et al., 1995; Vauclair, 1996; Peter, 1996*], but it is not the scope of this paper to review them. It is possible that the acceleration of the solar wind and the formation of a FIP bias are two independent issues, and the fact that both of these processes are differentiated between fast and slow solar wind is accidental. We, however, interpret these differences within the context of an overriding source differentiation between fast and slow solar wind [*Fisk et al., 1999b*].

The model of Fisk invokes differential rotation of the photosphere, superradial expansion beneath the source surface of the heliospheric magnetic field, and a symmetry axis of coronal holes offset from the Sun’s rotation axis to explain the motion of magnetic field footpoints on the source surface in the equatorially corotating reference frame. An immediate

requirement of the model is the continuous reorganization of open magnetic field in the low-latitude region of large coronal loops. Fast, coronal hole associated solar wind is then formed on field lines emanating from coronal holes, while slow solar wind is formed from material initially stored on large coronal loops that are forced open through reconnection as open magnetic field lines are moved into and migrating within the low-latitude region [see *Fisk et al.*, 1999b, Figure 3].

The fact that we observe a stronger bias of low-FIP elements in the slow solar wind rather than in the fast solar wind may be interpreted in terms of a recent model for elemental fractionation [*Schwadron et al.*, 1999]. In this model, wave heating on large coronal loops causes low-FIP elements that are predominantly ionized close to the transition region to have much larger scale heights than high-FIP elements that are predominantly neutral close to the transition region. The slow solar wind may well be formed from an array of loops with differing temperatures and heights. As discussed in section 3.3, the charge state data in slow solar wind supports this view. Since the low-FIP enhancements in the model of *Schwadron et al.* [1999] are intrinsically tied to the loop size and conditions on the loop, a large variability in the elemental fractionation would naturally be predicted. This large variability is clearly observed in the slow solar wind (see Plate 4). The hypothesis then that slow solar wind is formed from large coronal loops that are wave heated is consistent with the large composition variability in slow solar wind and compositional differentiation between fast and slow solar wind. These observational results are not, however, definitive proof of the hypothesis. Nonetheless, any theory for elemental fractionation in the slow solar wind must contend with them.

Fast solar wind emanates from coronal holes where large loops are rare. Hence the observation of an FIP effect in fast solar wind would suggest a mechanism occurring on small loops or well below the transition region. Such a mechanism has been presented by *von Steiger and Geiss* [1989] in which the fractionation occurs beneath the transition region, in the upper chromosphere, where large gradients across field lines are likely to exist. In this case the scale size for variability is set by the scale length associated with gradients across field lines, and this scale size would naturally be much smaller than those scale sizes associated with the loops from which the slow solar wind is presumably formed. The fact that the variability in the fast solar wind is smaller than in the slow solar wind is then consistent with elemental fractionation occurring on smaller scale lengths.

It must be emphasized that interpretations other than the one stated above cannot be excluded. The interpretation discussed here does, however, provide a context in which to understand the observations presented in this paper. This interpretation may also be tested from different observational vantage points. For example, spectroscopic results of *Feldman* [1998] using Solar and Heliospheric Observatory (SOHO)/Solar Ultraviolet Measurements of Emitted Radi-

ation (SUMER) data have been used to give evidence that strong biases of low-FIP elements relative to photospheric abundances occur on large coronal loops where plasma is stored long enough (of the order of days) to form the strong FIP biases observed in the slow solar wind.

5. Summary and Conclusions

Based exclusively on data obtained with the SWICS instrument on Ulysses, we have established long-term averages of element and charge state composition obtained in the two quasi-stationary solar wind types. Considering abundances of only the most reliably determined elements (C, O, Si, and Fe), it is clear that the FIP fractionation is present both in the slow wind and in the fast wind. However, the strength of the FIP bias is near the low end of previous reports in the slow solar wind, only a factor of 2.5 or 3 (depending on the adopted values for the photospheric composition). In fast streams the factor is yet lower but still significantly larger than 1. This indicates that the FIP fractionation effect is active also in the chromosphere beneath coronal holes, if only at a reduced strength.

The charge state distribution spectra also differ strongly between the two solar wind types. Thermal spectra prevail in fast streams, indicating a simple freezing-in process, but these are replaced with more complicated spectra that show an excess of high charge states in the slow wind, indicating a source that may be made up of sporadically opened loops that have a whole range of different temperatures.

Taken together, these results prove the fundamental difference between the two solar wind types and indicate that different physical processes have to be invoked to explain the heating and acceleration of either one. Indeed, models of elemental fraction and models of solar wind acceleration must contend with these observations.

Composition measurements of recently launched spacecraft are needed to improve that picture and will likely do so in the near future. The SWICS instrument on ACE [*Gloeckler et al.*, 1998] is identical to Ulysses/SWICS except for an improved data processing unit (DPU) and a significantly higher data rate, allowing one to exploit the full time resolution of 12 min as there is no need to accumulate multiple spectra. SOHO/Charge, Element, and Isotope Analysis System (CELIAS) [*Hovestadt et al.*, 1995] also has an improved time resolution even down to 5 min and, in addition, is also able to detect elements that are not accessible to SWICS-type instruments. It will be a vital test to the ideas regarding the FIP effect when reliable abundance measurements of such elements, for example, Na or Al, become available.

Appendix A: SWICS Data Analysis Techniques

In this paper we have given the first comprehensive report of all heavy ions that can be measured by SWICS in the solar wind. It therefore seems appropriate to give, in addition to the outline in the main body of the paper, a detailed account of the methods used for the analysis of the SWICS data in this appendix. The presentation of these methods is intended to be sufficiently general so as to be of interest for application to other time of flight instruments.

Despite its name, SWICS has also made important contributions to other aspects of heliospheric physics, in particular, through the discovery of interstellar and inner source pickup ions [Gloeckler and Geiss, 1998b, and references therein]. Unlike the solar wind ions, these ions are measured in double coincidence, and different methods and tools are required for their analysis; see Gloeckler and Geiss [1998a] for a summary of the steps involved.

The principle of operation of the SWICS instrument is as follows [Gloeckler et al., 1992]:

1. Ions with energy E , mass m , and charge q enter the instrument through a collimator.
2. The ions then pass through an electrostatic deflection system that serves as an energy-per-charge E/q filter.
3. Next the ions are postaccelerated as they cross a V_a potential voltage drop before entering the time-of-flight system.
4. In the time-of-flight system the ions first cross a thin carbon foil ($\sim 2.5 \mu\text{g cm}^{-2}$), triggering a start signal, travel a distance of $d \sim 10$ cm, and hit a solid state detector, triggering a stop signal, from which the travel time τ of the particle is determined.
5. Finally, the ions enter the gold-plated silicon solid state detector where their residual energy ε is measured.

The time of flight is thus given by

$$\tau = d / \sqrt{2(V_a + E/q - V_L)q/m}, \quad (\text{A1})$$

where V_L accounts for a small energy loss in the carbon foil. (V_L was found to be roughly proportional to the ion energy in the range relevant to the solar wind, which in turn is mainly determined by V_a , hence the expression as a potential.) The measured energy takes the form

$$\varepsilon = \alpha q(V_a + E/q - V_L) = \alpha m(d/\tau)^2/2, \quad (\text{A2})$$

where α is the nuclear defect, or pulse height defect, in the solid state detector [Ipavich et al., 1978].

There are three parameters which comprise an ion measurement, or pulse height analysis (PHA) event: E/q , τ , and ε . These quantities must be used to classify an ion's atomic mass M , mass-per-charge M/Q (the capitals indicate that these variables are expressed in amu and amu e^{-1} , respectively; E/q is expressed in keV e^{-1}), and subsequently its speed, $v[\text{km s}^{-1}] = 439\sqrt{(E/q)/(M/Q)}$.

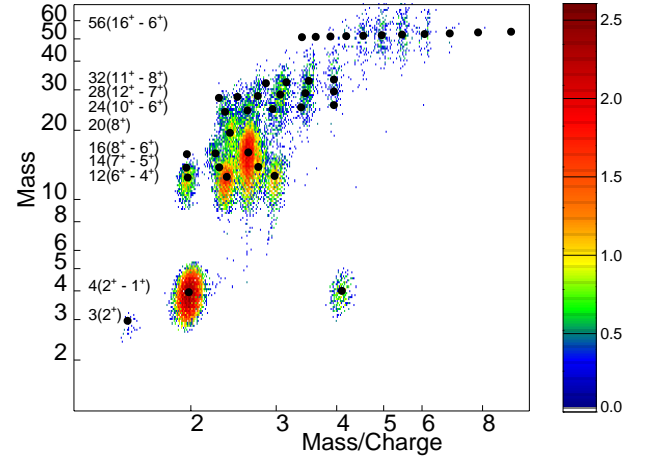


Plate A1. Ion counts accumulated over 10 days and plotted according to their mass and mass-per-charge derived from the approximate forward model of the on-board electronics. The color coding indicates the number of measurements on a logarithmic scale, and the black dots mark the nominal positions of 39 ion species, marked at left in the format $M(Q_{\max} - Q_{\min})$.

The analysis of SWICS PHA data proceeds in several steps, each of which will be discussed in a subsection below.

1. First, each PHA word, i. e., each event characterized by an energy-per-charge, E/q , a time-of-flight, τ , and an energy measurement, ε , is classified as an ion species. This may be done using the approximate on-board algorithm or, as we have done here, by an improved forward model.

2. Next, the number of events attributed to each ion species obtained during a fixed time (e. g., one or several spacecraft spins for each E/q value, see below) can be determined, the ion count rates. These rates must then be reduced to account for several selection and spillover effects, which in itself is a multistep process.

3. Finally, the ion rates can be converted to physical parameters according to (1)–(2), using calibrated values for the geometry factor and the detector efficiencies, and taking into account the duty cycle, i. e., the fact that the spacecraft rotates and SWICS only “sees” the solar wind during a fraction of each spin.

A1. Forward Model

In this subsection we first present an algorithm for calculating approximate values of the atomic mass \overline{M} and mass-per-charge $\overline{M/Q}$ for a given measurement parameterized by $(E/q, \tau, \varepsilon)$ [Gloeckler, 1977; Ipavich et al., 1978; Gloeckler and Hsieh, 1979]. This is the algorithm that is programmed into the on-board electronics, and it yields a mapping between a measurement and its mass/mass-per-charge approximations: $(E/q, \tau, \varepsilon) \mapsto (\overline{M/Q}, \overline{M})$. This representation of measurements is visualized in Plate A1. The mass/mass-per-charge algorithm used there and described below serves as a

good first approximation for the ion mass and charge state associated with a given measurement.

A more accurate method of separating the atomic species and charge states of a set of measurements involves the use of a forward model which is described in section A1.2. The forward model operates not in the $(M, M/Q)$ plane but in the (τ, ε) plane. This may seem like a disadvantage at first, as the position of each ion peak in that plane also depends on the E/q value, and thus we have to consider one (τ, ε) matrix for each E/q value instead of a single $(M, M/Q)$ matrix. This is outweighed by two advantages, though: (1) The resolution of neighboring peaks is improved, since the peak locations in the $(M, M/Q)$ matrix were still slightly dependent on E/q , which caused some blurring, and (2) the ion peaks in the (τ, ε) plane are better approximated by Gaussians than they are in the $(M, M/Q)$ plane. Thus the forward model effectively predicts a mapping of the ion properties $(E/q, M, Q)$ to the measured peak locations (τ_F, ε_F) and peak widths $(\sigma_\tau, \sigma_\varepsilon)$.

A1.1. Mass/mass-per-charge algorithm. The algorithm presented here provides an approximation for the ion atomic mass \overline{M} and ion mass-per-charge $\overline{M/Q}$ given a measurement parameterized by $(E/q, \tau, \varepsilon)$ [Gliem et al., 1988]. It follows naturally from the formulae describing the instrument operation (equations (A1) and (A2)). The form for the mass-per-charge approximation is clear from (A1):

$$\overline{M/Q} = \left(\frac{E/q + V_a - V_L}{H_0 U_0} \right) \left(\frac{\tau}{\tau_0} \right)^2. \quad (\text{A3})$$

Here we set $\tau_0 = 1$ ns and $U_0 = 1$ kV, and we have the calibrated values $H_0 = 52195$ and $V_L = 1.5$ kV. The postacceleration voltage can be selected by ground command but has remained fixed at $V_a = 22.875$ kV during the whole mission so far.

The form for the mass approximation \overline{M} is somewhat more complicated owing to nonlinear effects introduced by the nuclear defect in the solid-state detector. From (A2) we see that the ion mass approximation must depend directly on the solid-state detector energy measurement ε and the time of flight τ . The algorithm is then expressed as a polynomial fit involving these parameters:

$$\overline{M} = \exp \left(A_1 + A_2 X + A_3 Y + A_4 XY + A_5 X^2 + A_6 Y^3 \right), \quad (\text{A4})$$

where $X = \ln(\varepsilon/\varepsilon_0)$ with $\varepsilon_0 = 1$ kV and $Y = \ln(\tau/\tau_0)$. The polynomial coefficients obtained by calibration are $A_1 = 5.81090$, $A_2 = -1.50052$, $A_3 = -3.01352$, $A_4 = 0.47113$, $A_5 = 0.0804588$, and $A_6 = 0.0731559$.

A1.2. Ulysses/SWICS forward model. A forward model provides a prediction for the measured peak locations (τ_F, ε_F) and peak widths $(\sigma_\tau, \sigma_\varepsilon)$, given the ion properties $(E/q, M, Q)$: $(E/q, M, Q) \mapsto (\tau_F, \varepsilon_F, \sigma_\tau, \sigma_\varepsilon)$. In these coordinates the peaks can be approximated very well by Gaussians both in the τ direction and in the ε direction. Here we describe the procedure used for Ulysses/SWICS; a

similar approach has been used for SOHO/Charge Time of Flight (CTOF) by *Hefti* [1997].

The mass/mass-per-charge algorithm provides an important approximation for the peak locations in the $(M, M/Q)$ coordinates. By inverting the algorithm we obtain a first, approximate forward model, i.e., a mapping between the ion properties $(E/q, M, Q)$ and approximate peak locations $(\overline{\tau}, \overline{\varepsilon})$, $(E/q, M, Q) \mapsto (\overline{\tau}, \overline{\varepsilon})$:

$$\overline{\tau}/\tau_0 = \sqrt{\frac{H_0 M/Q U_0}{E/q + V_a - V_L}}, \quad (\text{A5})$$

$$\overline{\varepsilon}/\varepsilon_0 = \exp \left(\frac{-\beta + \sqrt{\beta^2 - 4\alpha\gamma}}{2\alpha} \right). \quad (\text{A6})$$

Here $\alpha = A_5$, $\beta = A_2 + A_4 \overline{Y}$, $\gamma = A_1 + \overline{Y}(A_3 + A_6 \overline{Y}^2) - \ln(M)$, and again $\overline{Y} = \ln(\overline{\tau}/\tau_0)$. For reference, we call this the “MMQ-forward model.” Comparisons between the MMQ-forward model peak locations and the measured peak locations from flight data reveal systematic differences.

A straightforward way to improve the MMQ-forward model is to perturb, or “tune,” the constants until the measured peak locations are reproduced. For the time of flight position, the constants H_0 and V_L in the MMQ-forward model have been replaced by $H_1(M)$ and $U_L(M)$, which depend on atomic species. The corrected energy position ε_F is a linear perturbation of $\overline{\varepsilon}$. For the peak widths we found that, some scatter notwithstanding, σ_τ/τ_F is a constant and that σ_ε is a power law function of the ion speed [Oetliker, 1993]. Thus the improved forward model is parameterized as follows:

$$\tau_F/\tau_0 = \sqrt{\frac{H_1(M) M/Q U_0}{E/q + V_a - U_L(M)}}, \quad (\text{A7})$$

$$\varepsilon_F/\varepsilon_0 = H_3(M) + H_4(M) \overline{\varepsilon}/\varepsilon_0, \quad (\text{A8})$$

$$\sigma_\tau/\tau_F = H_2(M), \quad (\text{A9})$$

$$\sigma_\varepsilon/\varepsilon_F = H_5(M) \left(\frac{E/q + V_a}{M/Q U_0} \right)^{H_6(M)}. \quad (\text{A10})$$

For every atomic species we have seven constants, which depend only on the ion mass, to tune the model, $H_1(M)$, $H_2(M)$, \dots , $H_6(M)$, and $U_L(M)$. This parameterization is somewhat simpler than the one used by *Wimmer-Schwein-gruber* [1994], who took the peaks to be asymmetric, with unequal widths above and below the center. However, we found that the peaks can equally well be represented by symmetric Gaussians, and we therefore preferred the simpler, symmetric approach. We also experimented with kappa distributions for describing the ion peaks, but again the improvement of the obtained fit, if any, did not justify the associated increase in the number of parameters.

We then used the massive amounts of in-flight data to accumulate (τ, ε) matrices for each E/q step over long time periods and to measure the location and width of each visible ion peak in every one such matrix, given in Figure A1.

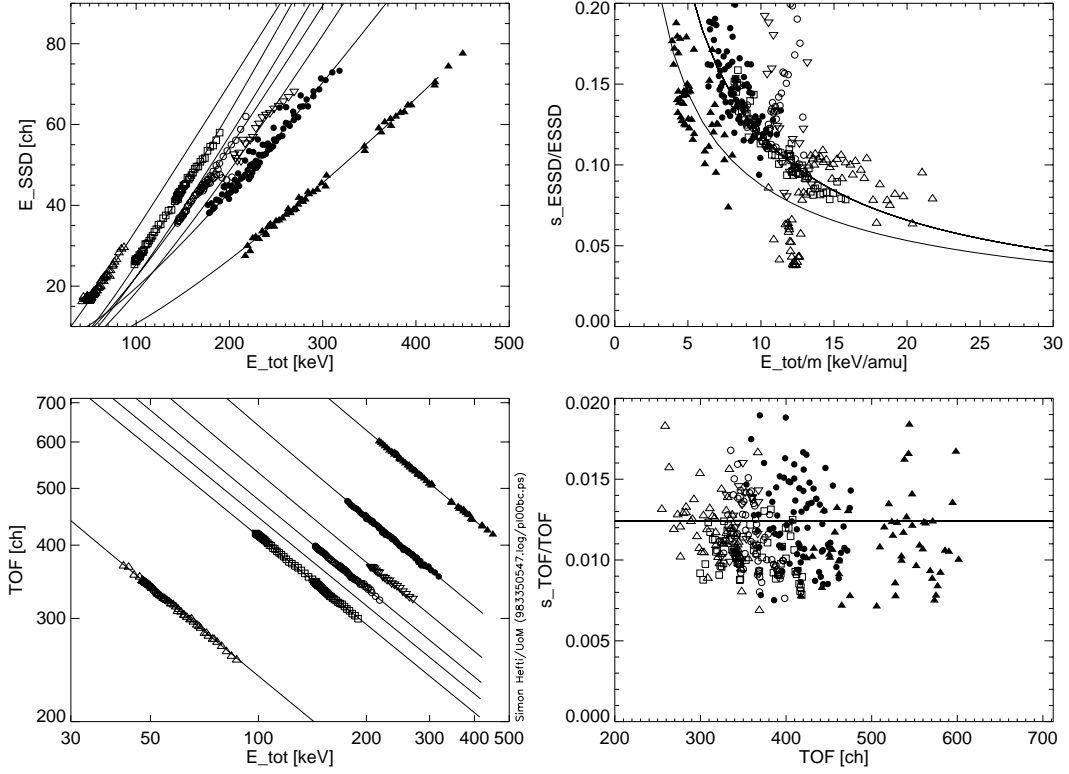


Figure A1. Forward model parameters of Ulysses/SWICS. We plot here the observed peak locations (left) and peak widths (right) in the energy (top) and time of flight (bottom) directions for helium (triangles), carbon (squares), oxygen (circles), neon (inverted triangles), silicon (solid circles), and iron (solid triangles). The curves indicate the forward model predictions. Here $E_{\text{tot}} = q(E/q + V_a)$ denotes the incident ion energy, $\text{TOF} = (\tau_F/\tau_0)(1023/200)$ denotes the time of flight in channel units, $E_{\text{SSD}} = (\varepsilon_F/\varepsilon_0)(255/610.78)$ denotes the energy measured at the solid state detector in channel units, and s_{TOF} and s_{ESSD} denotes the widths of the peaks in the time of flight, σ_τ , and energy, σ_ε , directions.

The model parameters were finally obtained from the peak locations by a least squares fit to the observations; they are listed in Table A1. In Plate A2 we show an example of one such (τ, ε) matrix, taken at $E/q = 8.71$ keV/e, along with the forward model predictions. It is evident that the forward model reproduces the peak locations and the peak widths quite successfully.

A2. Rate Reduction

In this section we outline a technique for obtaining the rates for individual ion species, given a set of instrument measurements or events. The term rate refers to counts measured during a given time period, i.e., a single spacecraft spin or, more often, a number of spins with the same associated E/q value. In the normal mode of instrument operation the energy-per-charge is held fixed $E/q = E/q|_i$ at each step i for the duration of a single spacecraft rotation ~ 12 s, and it is stepped in 64 logarithmic steps from 60 down to $0.6 \text{ keV } q^{-1}$ (the E/q resolution is thus some 7.3%; the energy passband of each E/q step is $\Delta(E/q)/(E/q) = 4.3\%$ [von Steiger, 1995]).

The goal then is to find the number of ions N_{si} for a given species s at a given energy-per-charge step $E/q = E/q|_i$ ac-

cumulated over n_{cyc} instrument cycles. The species s refers to an ion with atomic mass M in atomic mass units and charge state Q in units of the elementary charge. The challenge presented here is to obtain a reliable inversion method for quite low statistics, when a fitting technique to the measured distributions (shown in Plate A2) would fail.

The basic ingredient at this point is the forward model described above. Given the ion characteristics $(E/q, M, Q)$, it predicts the mapping $(E/q, M, Q) \mapsto (\tau_F, \varepsilon_F, \sigma_\tau, \sigma_\varepsilon)$. As a matter of notation, we denote the forward model peak location for species s at energy-per-charge step i by $(\tau_F^i, \varepsilon_F^i)$, and we denote the forward model peak widths by $(\sigma_\tau^i, \sigma_\varepsilon^i)$.

In the following discussion we imagine a set of n_i measurements or events $(\tau_{ij}, \varepsilon_{ij})$ at energy-per-charge step i with the index j running through the measurement set $j = 1 \dots n_i$. We will then describe a technique for obtaining the rates N_{si} with five steps. Each of the steps is described in sections A2.1–A2.5.

A2.1. Step 1: Box rates. By simply counting the number of measurements which fall into a rectangular box within one standard deviation in either direction of a peak location for species s , the box count rate C_{si} is obtained. More specif-

Table A1. Ulysses/SWICS Forward Model Constants

M	H_1 , kV	U_L , kV	H_2	H_3	H_4	H_5	H_6
4.0	54329.2	0.34	0.0124	8.302	0.815	0.84	-0.85
12.0	54675.7	0.00	0.0124	1.847	1.023	0.84	-0.85
14.0	54312.9	0.00	0.0124	0.000	1.000	0.84	-0.85
16.0	54201.8	0.14	0.0124	5.322	0.965	0.84	-0.85
20.0	52794.6	0.29	0.0124	2.395	1.000	0.84	-0.85
28.0	53360.2	0.50	0.0124	16.347	0.929	0.84	-0.85
56.0	52281.9	0.64	0.0124	7.475	0.933	0.46	-0.72

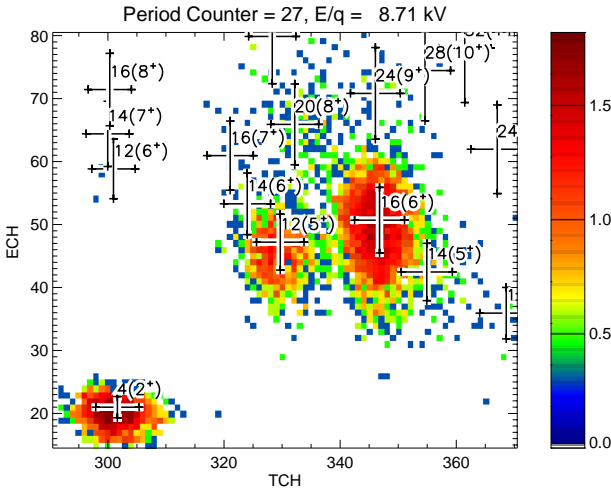


Plate A2. Ion counts made by Ulysses/SWICS, accumulated over 10 days and binned in terms of time of flight, TCH, and solid state detector energy, ECH, in “channel” units (compare caption to Figure A1). The color coding indicates the number of measurements on a logarithmic scale. Forward model predictions are also shown with their associated standard deviations. The labels of these forward model predictions include the ion mass and charge state in parentheses: For example, carbon-5⁺ has the label 12(5⁺). At this step, the energy-per-charge is given by $E/q = 8.71$ kV/e.

ically,

$$C_{si} = \sum_{j=1}^{n_i} \theta \left(\sigma_{\tau}^{si} - \left| \tau_{ij} - \tau_F^{si} \right| \right) \theta \left(\sigma_{\varepsilon}^{si} - \left| \varepsilon_{ij} - \varepsilon_F^{si} \right| \right), \quad (\text{A11})$$

where $\theta(x)$ is the Heaviside step function: $\theta(x > 0) = 1$ and $\theta(x < 0) = 0$.

If the measurements are distributed as Gaussians and the forward model characterizes them accurately, the box rate C_{si} counts $\text{erf}(1/\sqrt{2})^2 = 47\%$ of the ions in species s at step i , i.e., the square of the 68% inside a 1- σ neighborhood of a one-dimensional (1-D) Gaussian. (Alternatively, an elliptic region around $(\tau_F^{si}, \varepsilon_F^{si})$ may be used instead of a rectangle, in which case 39% of the ions would fall inside.)

A2.2. Step 2: Basic rate correction. Not all ion events measured by Ulysses/SWICS are assigned equal priority. Telemetry is limited, and solar wind protons and helium are much more abundant than solar wind heavy ions. This being the case, measurements consistent with heavy ($M > 8.5$) solar wind ions are given higher priority for telemetry, and heavy pickup ions are given highest priority. In other words, a prioritization scheme is implemented for data transmission and must be corrected for in the analysis.

This can be done by using the basic rates, R_{ik} , that are transmitted for each step i and priority range k . We have $k = 1, 2$, or 3 for protons and alpha particles, heavy solar wind ions, and heavy pickup ions, respectively. The basic-rate weighted box rates, B_{si} , are calculated from the box count rates, C_{si} , by

$$B_{si} = \frac{R_{ik(s)}}{N_{ik(s)}} C_{si}, \quad (\text{A12})$$

where $N_{ik(s)}$ is the actual number of transmitted events in step i from priority range k , which in turn depends on the species s under consideration, and $B_{ik(s)}$ is the corresponding total number of measured events. Since $N_{ik(s)}$ may be zero for an individual step i when $B_{ik(s)}$ is not, it is advisable to accumulate both R and N over a number of steps to form an average basic-rate correction factor over the chosen accumulation time.

Note that the correction factor is the same for all events in one step i and one priority range k . It therefore does not affect the solar wind heavy ion abundance ratios but only the absolute values and the ratios to protons and alpha particles.

A2.3. Step 3: Spillover correction. The distributions of multiple ion species evidently overlap. This can be seen for example for C⁵⁺ and O⁶⁺ in Plate A2. Therefore the box rates are of limited use without a correction scheme that accounts for the overlap of measured distributions, or equivalently, “spillover,” of multiple species.

Consider the approximation that each species produces a measurement distribution with the form of a two-dimension-

al (2-D) Gaussian:

$$G_{si}(\tau, \varepsilon) = \frac{1}{2\pi\sqrt{\sigma_\tau^{si}\sigma_\varepsilon^{si}}} \cdot \exp\left[-\frac{(\tau - \tau_F^{si})^2}{2(\sigma_\tau^{si})^2} - \frac{(\varepsilon - \varepsilon_F^{si})^2}{2(\sigma_\varepsilon^{si})^2}\right]. \quad (\text{A13})$$

At step i the fraction of species t ions which are measured within one standard deviation of the species s measurement location is given by

$$\begin{aligned} S_{st}^i &= \int_{\varepsilon_F^{si}-\sigma_\varepsilon^{si}}^{\varepsilon_F^{si}+\sigma_\varepsilon^{si}} d\varepsilon \int_{\tau_F^{si}-\sigma_\tau^{si}}^{\tau_F^{si}+\sigma_\tau^{si}} d\tau G_{ti}(\tau, \varepsilon) \\ &= \frac{1}{2} \left[\operatorname{erf}\left(\frac{\tau_F^{si} + \sigma_\tau^{si} - \tau_F^{ti}}{\sqrt{2}\sigma_\tau^{ti}}\right) - \operatorname{erf}\left(\frac{\tau_F^{si} - \sigma_\tau^{si} - \tau_F^{ti}}{\sqrt{2}\sigma_\tau^{ti}}\right) \right] \\ &\quad \cdot \frac{1}{2} \left[\operatorname{erf}\left(\frac{\varepsilon_F^{si} + \sigma_\varepsilon^{si} - \varepsilon_F^{ti}}{\sqrt{2}\sigma_\varepsilon^{ti}}\right) - \operatorname{erf}\left(\frac{\varepsilon_F^{si} - \sigma_\varepsilon^{si} - \varepsilon_F^{ti}}{\sqrt{2}\sigma_\varepsilon^{ti}}\right) \right]. \end{aligned} \quad (\text{A14})$$

Here $\operatorname{erf}(x) = 2/\sqrt{\pi} \int_0^x dt \exp(-t^2)$ is the error function. Recall from above that $S_{ss}^i = 47\%$.

The set of matrices S^i are referred to as spillover matrices. They describe the contribution of each ion species t into the box around the location of species s ; that is, satisfy the following equation

$$B_{si} = \sum_{t=1}^{n_{\text{ion}}} S_{st}^i N_{ti} \quad (\text{A15})$$

where n_{ion} is the number of ion species considered. By inverting (A15) we obtain the estimate for the rates N_{si}^{spill} ,

$$N_{si}^{\text{spill}} = \sum_{t=1}^{n_{\text{ion}}} (S^i)^{-1}_{st} B_{ti}, \quad (\text{A16})$$

which accounts only for those events in the box around species s that were, in fact, caused by species s .

A2.4. Step 4: Correcting ghost counts. One of the drawbacks of this scheme is the fact that N_{si}^{spill} is not positive definite, even though S^i is. Negative elements of N_{si}^{spill} play the role of ghost ions: A negative solution for one species is compensated by extraneous positive contributions in the neighboring species. Therefore, if the negative solutions were simply thrown out, the total number of solution counts, \tilde{n}_i , would be greater than the true total number of measured counts, n_i , an unphysical situation:

$$\tilde{n}_i = \sum_{t=1}^{n_{\text{ion}}} \theta(N_{ti}^{\text{spill}}) N_{ti}^{\text{spill}} > n_i. \quad (\text{A17})$$

Ghost counts are unphysical since they artificially increase the counts of neighboring ions, but they may be easily corrected. The procedure is to identify, in each step i , those species, \tilde{s} , for which a negative result is obtained from the spillover correction, $N_{\tilde{s}i}^{\text{spill}} < 0$. Subsequently, their original box rates, $B_{\tilde{s}i} \mapsto \tilde{B}_{\tilde{s}i}$, are revised such that the corresponding spillover rate will be identically zero, $\tilde{N}_{\tilde{s}i}^{\text{spill}} = 0$. Hence, $\tilde{B}_{\tilde{s}i}$ may be obtained from the requirement

$$(S^i)^{-1}_{\tilde{s}\tilde{s}} \tilde{B}_{\tilde{s}i} + \sum_{t \neq \tilde{s}} (S^i)^{-1}_{\tilde{s}t} B_{ti} = 0. \quad (\text{A18})$$

With the revised box rates in hand, revised values of the spillover rates may be calculated which are not infiltrated by ghost counts:

$$\tilde{N}_{si}^{\text{spill}} = \sum_{t=1}^{n_{\text{ion}}} (S^i)^{-1}_{st} [B_{ti} \theta(N_{ti}^{\text{spill}}) + \tilde{B}_{ti} \theta(-N_{ti}^{\text{spill}})]. \quad (\text{A19})$$

This correction scheme is exactly equivalent to temporarily removing species \tilde{s} from consideration altogether during step i , while it has the advantage that the decision of which species to remove is not needed when the rates are accumulated, but can be done a posteriori.

A2.5. Step 5: Probabilistic assignments. Up to this point, we have not considered counts outside the 1-sigma range of each ion species. This is not ideal considering the low statistics available, particularly, for the species with low abundances. The rates, which have now undergone a spillover correction and a negative count correction, serve as a good initial guess for the true rates. Given these rates, we now obtain the true rates by a probabilistic procedure: For each ion event, (τ, ε) at step i , we define the probability that it corresponds to species s as

$$P_{si}(\tau, \varepsilon) = \frac{\tilde{N}_{si}^{\text{spill}} G_{si}(\tau, \varepsilon)}{\sum_{t=1}^{n_{\text{ion}}} \tilde{N}_{ti}^{\text{spill}} G_{ti}(\tau, \varepsilon)}, \quad (\text{A20})$$

with $G_{si}(\tau, \varepsilon)$ from (A13). We then attribute to it a unique identity by generating a random number, and we assign the event to species s with probability P_{si} . Proceeding in this way with all events finally produces the rates of all species s in step i .

The probabilistic assignment has a number of distinct advantages. First of all, it exploits all available events and makes the optimum guess for the identity of each one of them. Moreover, it will obviously remain stable even at very low statistics, as there are no iterative or fitting procedures involved. Finally, it can handle situations in which ion peaks are distorted, for example, due to differential linearity in the analog-to-digital converters. This effect preferentially attributes events to specific columns (or rows) in the (τ, ε) matrix, at the expense of neighboring ones. A simple scheme that counts events inside a box is strongly dependent on whether such a column (or row) lies just inside

or outside of the box, whereas the probabilistic assignment scheme is much more tolerant and will attribute most counts to the correct species even in that situation. For completeness, we write down the deduced rate of species s based on the probabilistic assignment at step i :

$$N_{si}^{\text{prob}} = \sum_{j=1}^{n_i} P_{si}(\tau_{ij}, \varepsilon_{ij}). \quad (\text{A21})$$

A3. Observed Distribution Function

In order to derive observables such as density, velocity, or temperature of an ion species from the measurements, the rates must first be translated into physical quantities such as differential fluxes or distribution functions, i. e., phase space density as a function of energy or velocity (compare equations 1–2)). This step is generally straightforward, but care must be taken to properly interpret these quantities for the low-energy ions observed by SWICS. In this section we will discuss these issues as they relate to Ulysses/SWICS.

The observed counts for species s at step i , N_{si} , can be related to the distribution function f as follows:

$$N_{si} = \frac{\eta_{si} g t_{\text{acc}}}{2\pi} \int_0^{2\pi} d\phi \int_{(\phi)} d\Omega_{\text{col}} \int d^3v' |\mathbf{v}' \cdot \hat{\mathbf{e}}_{\text{col}}| \cdot \theta(\Delta v'_i/2 - |v - v'_i|) \delta^2(\hat{\mathbf{e}}_v + \hat{\mathbf{e}}_{\text{col}}) f(\mathbf{v}'). \quad (\text{A22})$$

In this expression, η_{si} is the detection efficiency of species s at step i (see below), g is the geometric factor for a pure pencil beam, and t_{acc} is the accumulation time. For Ulysses/SWICS we have calibrated $g = 0.0185 \text{ cm}^2$ [von Steiger, 1995], and $t_{\text{acc}} = n_{\text{cyc}} t_{\text{spin}}$ where $t_{\text{spin}} = 12 \text{ s}$ is the spin period of Ulysses.

The unit normal to the instrument collimator is denoted by $\hat{\mathbf{e}}_{\text{col}}$ (its sign is chosen such that it is directed away from the sensor), and the operator $\int_{(\phi)} d\Omega_{\text{col}}$ integrates $\hat{\mathbf{e}}_{\text{col}}$ over the acceptance solid angle of the collimator. The geometrical orientation of the collimator is defined below. In a coordinate system centered about the collimator symmetry axis (the collimator coordinates), the angular integral may be written as

$$\int_{(\phi)} d\Omega_{\text{col}} = \int_{\pi-\Delta\phi_c}^{\pi} d\phi_c \int_{\gamma-\Delta\theta_c/2}^{\gamma+\Delta\theta_c/2} d\theta_c \sin\theta_c, \quad (\text{A23})$$

where $\gamma = 57^\circ$, $\Delta\theta_c = 4^\circ$, and $\Delta\phi_c = 69^\circ$.

Note that acceptance angles are fixed, but the collimator orientation depends on the spin azimuth, ϕ , which makes the integral in (A23) dependent on ϕ . Therefore, during a given spin, the collimator acceptance angles are averaged over the spacecraft spin orientations $(1/2\pi) \int_0^{2\pi} d\phi \int_{(\phi)} d\Omega_{\text{col}} \dots$. The function of the collimator is to accept only ions with velocities, \mathbf{v}' , directed antiparallel to $\hat{\mathbf{e}}_{\text{col}}$. Mathematically, this effect is captured by the 2-D Dirac delta function, $\delta^2(\hat{\mathbf{e}}_v + \hat{\mathbf{e}}_{\text{col}})$, which has units of sr^{-1} .

Given an energy-per-charge acceptance window at step i , $\Delta E/q|_i$ (recall that $\Delta E/q|_i = 0.043 E/q|_i$), the deflection system only accepts ions with speeds in the range

$|v' - v'_i| \leq \Delta v'_i/2$, where $v'_i = \sqrt{2(q/m)E/q|_i}$ and $v'_i \Delta v'_i = (q/m)\Delta E/q|_i$. This effect is captured in (A22) by the step function $\theta(\Delta v'_i/2 - |v - v'_i|)$.

Although (A22) includes all the instrumental effects, it is of little utility because it does not provide a simple algebraic expression which relates the counts to a physical quantity. For this purpose, we introduce the observed distribution function, $\tilde{f}(v')$, which is defined as

$$\tilde{f}(v') = \frac{1}{2\pi} \int_0^{2\pi} d\phi \int_{(\phi)} d\Omega_{\text{col}} f(\mathbf{v}'). \quad (\text{A24})$$

with $\mathbf{v}' = -v'\hat{\mathbf{e}}_{\text{col}}$. The observed distribution function carries with it the angular integrations performed implicitly by the collimator and spacecraft spin. It may be related to the measured counts simply as

$$N_{si} = \eta_{si} g \tau_a 2(q/m)^2 E/q|_i \Delta E/q|_i \tilde{f}(v'_i). \quad (\text{A25})$$

Note that the integral over ion speed $\int_{v'_i-\Delta v'_i/2}^{v'_i+\Delta v'_i/2} dv'(v')^3$ has been rewritten as $2(q/m)^2 E/q|_i \Delta E/q|_i$.

The observed, one-dimensional distribution is related to the full, three-dimensional distribution function in (A24). The transformation is complicated, however, and it is desirable and necessary to develop a simple scheme for the extraction of ion densities directly from the observed distributions. The scheme relies on the assumption that the true distribution functions are essentially Gaussian in form; it is therefore only applicable to solar wind ions. Different schemes may be devised for other ion populations simply by making different assumptions for the shape of the full distribution function.

Consider the transformation of a three-dimensional Gaussian distribution function,

$$f(\mathbf{v}') = n \left(2\pi v_{\text{th}}^2\right)^{-3/2} \exp\left[-\frac{(\mathbf{v}' - \mathbf{v}_0)^2}{2v_{\text{th}}^2}\right], \quad (\text{A26})$$

to an observed distribution function, $\tilde{f}(v')$. Here the density is given by n , the thermal speed is given by v_{th} , and the solar wind velocity is given by \mathbf{v}_0 . The result of the transformation of (A24) can be written as

$$\tilde{f}(v') = n \frac{D(\alpha, \Delta\Psi)}{\sqrt{2\pi} v' v_0 v_{\text{th}}} \exp\left[-\frac{(v' - v_0)^2}{2v_{\text{th}}^2}\right], \quad (\text{A27})$$

where the Mach angle is defined as $\Delta\Psi = v_{\text{th}}/\sqrt{v'v_0} \approx v_{\text{th}}/v_0$ and α is the aspect angle, or equivalently, the Sun-Probe-Earth angle. The difficulty has simply been shifted into the function $D(\alpha, \Delta\Psi)$, the duty cycle.

A3.1. Duty cycle. The factor $D(\alpha, \Delta\Psi)$ folds in all the angular integrations performed implicitly by the instrument:

$$D(\alpha, \Delta\Psi) = \frac{1}{2\pi} \int_0^{2\pi} d\phi \int_{(\phi)} d\Omega_{\text{col}} \cdot \frac{1}{2\pi(\Delta\Psi)^2} \exp\left[-\frac{1 - \cos\Psi}{(\Delta\Psi)^2}\right], \quad (\text{A28})$$

where Ψ is the angle between an individual ion velocity, \mathbf{v}' , and the solar wind velocity, \mathbf{v}_0 .

Typically, in the solar wind the Mach angle is small. For a pure pencil beam, $\Delta\Psi = 0$, calculation of $D(\alpha)$ reduces to a simple exercise in spherical trigonometry, with the result

$$D(\alpha) = \begin{cases} 1/2 & (\alpha \leq 2^\circ) \\ \frac{1}{2\pi} \left(\arccos \frac{\cos \alpha \cos \gamma - \cos \gamma_-}{\sin \alpha \sin \gamma} - \arccos \frac{\cos \alpha \cos \gamma - \cos \gamma_+}{\sin \alpha \sin \gamma} \right) & (\alpha > 2^\circ) \\ 0 & (\alpha > 56^\circ), \end{cases} \quad (\text{A29})$$

where $\gamma_{\pm} = \gamma \pm \Delta\theta_c/2$.

In the more general case, $\Delta\Psi \ll 1$, it is appropriate to expand $\cos \Psi$ as

$$1 - \cos \Psi \approx \frac{(\theta_c - \theta_{c0})^2}{2} + \sin^2 \theta_{c0} \frac{(\phi_c - \phi_{c0})^2}{2}, \quad (\text{A30})$$

where (θ_{c0}, ϕ_{c0}) are the polar and azimuthal angles of the solar wind in collimator coordinates. Expression (A30) is correct to third order with respect to the terms $(\theta_c - \theta_{c0})$ and $(\phi_c - \phi_{c0})$. Using this approximation and the integration limits in (A23), we obtain the following expression for the duty cycle:

$$D(\alpha, \Delta\Psi) = \frac{1}{2\pi} \int_0^{2\pi} d\phi \frac{1}{2} \left[\operatorname{erf} \left(\frac{\gamma - \theta_{c0} + \Delta\theta_c/2}{\sqrt{2}\Delta\Psi} \right) - \operatorname{erf} \left(\frac{\gamma - \theta_{c0} - \Delta\theta_c/2}{\sqrt{2}\Delta\Psi} \right) \right] \cdot \frac{1}{2} \left[\operatorname{erf} \left(\sin \theta_{c0} \frac{\pi - \phi_{c0}}{\sqrt{2}\Delta\Psi} \right) - \operatorname{erf} \left(\sin \theta_{c0} \frac{\pi - \phi_{c0} - \Delta\phi_c}{\sqrt{2}\Delta\Psi} \right) \right]. \quad (\text{A31})$$

In (A31), the solar wind direction specified by θ_{c0} and ϕ_{c0} may be determined using a rotation matrix, as follows; see Figure A2 for a sketch of the collimator geometry.

Let us start in the spacecraft coordinates. Here the spin axis, with associated unit vector $\hat{\mathbf{e}}_z$ (marked with a circled plus, \oplus , in Figure A2), is directed at Earth, and a vector directed at the Sun from the spacecraft $\hat{\mathbf{e}}_s$ (marked with a circled dot, \odot) lies completely in the x - z plane: $\hat{\mathbf{e}}_s = \hat{\mathbf{e}}_x \sin \alpha + \hat{\mathbf{e}}_z \cos \alpha$, where α is the aspect angle, or the Sun-Probe-Earth angle.

The collimator's symmetry axis $\hat{\mathbf{e}}_{z_c}$ (marked with a circled cross, \otimes) is offset from the spin axis by $\gamma = 57^\circ$. The actual orientation of the collimator's symmetry axis $\hat{\mathbf{e}}_{z_c}$ depends on the spin orientation ϕ of the instrument: in spacecraft coordinates the azimuthal angle of $\hat{\mathbf{e}}_{z_c}$ is given by $\phi_{z_c} = \phi - \phi_0$, where

$$\phi_0 = \arccos \left(\frac{\cos \gamma}{\sin \gamma} \frac{1 - \cos \alpha}{\sin \alpha} \right). \quad (\text{A32})$$

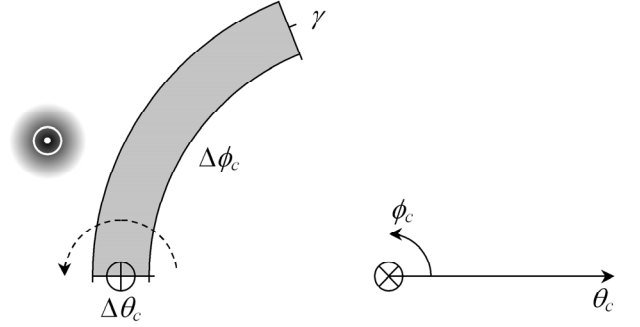


Figure A2. Sketch of the collimator geometry in collimator coordinates, (θ_c, ϕ_c) , with origin at the circled cross (not to scale). The collimator accepts ions from the shaded region, which is offset by an angle of $\gamma = 57^\circ$ from the origin, and subtends $\Delta\theta_c = 4^\circ$ in polar angle and $\Delta\phi_c = 69^\circ$ in azimuth. The collimator rotates in the direction indicated by the dashed arrow about the spacecraft spin axis, marked by the circled plus sign, which is always pointed towards Earth. The solar wind comes from an arbitrary direction, marked by the white circled dot, which is offset from the spin axis by the aspect angle, α (not shown), and may be blurred by the Mach angle, $\Delta\Psi$ (shaded). The duty cycle represents the portion of the spacecraft spin during which the solar wind may enter the collimator.

Consider a new coordinate system with a z_c axis given by $\hat{\mathbf{e}}_{z_c}$. The x_c axis of this system is oriented such that the spin axis $\hat{\mathbf{e}}_z$ lies in the x_c - z_c plane and the projection along the x_c axis is negative, $\hat{\mathbf{e}}_z \cdot \hat{\mathbf{e}}_{x_c} < 0$. This then uniquely defines “collimator coordinates.” In this coordinate system the collimator represents a cut from a spherical shell which has azimuthal angles ranging from $\phi_c = 180^\circ - \Delta\phi_c$ to $\phi_c = 180^\circ$ and polar angles ranging from $\theta_c = \gamma - \Delta\theta_c/2$ to $\theta_c = \gamma + \Delta\theta_c/2$. Recall that $\gamma = 57^\circ$, $\Delta\phi_c = 69^\circ$, and $\Delta\theta_c = 4^\circ$. Note that one side of the collimator is directed along the spin axis.

With the collimator coordinates well defined, it is straightforward to construct a transformation \mathbf{M} which when operating on a vector \mathbf{v} represented in spacecraft coordinates yields the vector representation in collimator coordinates \mathbf{v}_c : $\mathbf{M} \cdot \mathbf{v} = \mathbf{v}_c$, where

$$\mathbf{M} = \begin{bmatrix} \cos \gamma \cos \phi_{z_c} & \cos \gamma \sin \phi_{z_c} & -\sin \gamma \\ -\sin \phi_{z_c} & \cos \phi_{z_c} & 0 \\ \sin \gamma \cos \phi_{z_c} & \sin \gamma \sin \phi_{z_c} & \cos \gamma \end{bmatrix}. \quad (\text{A33})$$

The transpose of \mathbf{M} is also its inverse, $\mathbf{M}^{-1} = \mathbf{M}^T$, since the matrix only involves rotations and is therefore unitary. The resulting angles, θ_{c0} and ϕ_{c0} , of the solar wind direction are then given by

$$\begin{aligned} \cos \theta_{c0} &= \sin \gamma \cos(\phi - \phi_0) \sin \alpha + \cos \gamma \cos \alpha, \\ \sin \theta_{c0} \sin \phi_{c0} &= -\sin(\phi - \phi_0) \sin \alpha, \\ \sin \theta_{c0} \cos \phi_{c0} &= \cos \gamma \cos(\phi - \phi_0) \sin \alpha - \sin \gamma \cos \alpha. \end{aligned} \quad (\text{A34})$$

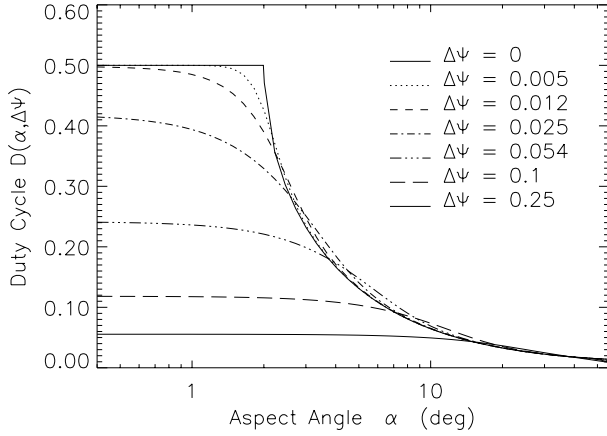


Figure A3. The duty cycle correction as a function of the aspect angle. The curves correspond to the indicated values of the solar wind Mach angle $\Delta\Psi$.

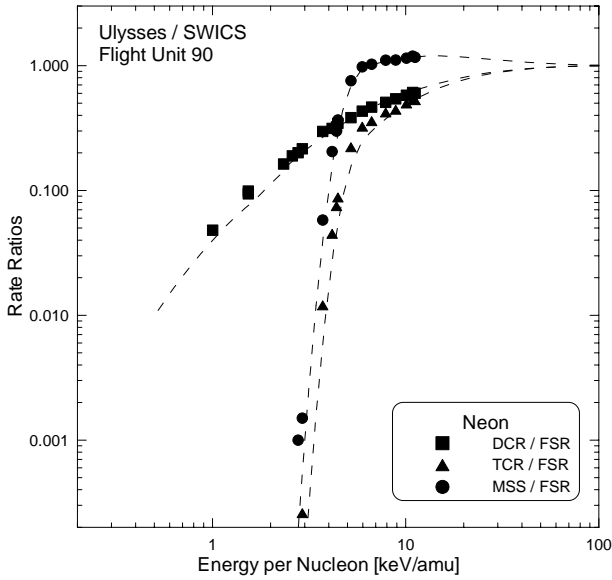


Figure A4. Ulysses/SWICS preflight calibration data of neon (solid symbols), expressed as ratios of the detector rates FSR (front rate), DCR (double coincidence rate), MSS (main solid state detector rate), and TCR (triple coincidence rate). The data are compared to a model for the detector efficiencies (dashed lines), plotted as a function of energy per nucleon. The model contains two free parameters that could be used to obtain a satisfactory fit with the data. The agreement was optimized in the range of the solar wind ions, around 12 keV amu^{-1} .

Finally, the resulting duty cycle $D(\alpha, \Delta\Psi)$ is plotted in Figure A3 for several values of the Mach angle.

A3.2. Detector efficiencies. Calibration data for Ulysses/SWICS have been taken at the University of Bern accelerator facility, CASYMS [Ghielmetti et al., 1983; Steinacher et al., 1995], in May 1990 (solid symbols in Figure A4). Efficiency data were taken for the elements H, He, C, O, Ne, Ar,

and Kr. Each calibration run consisted of an accumulation of the direct sensor rates during a number of instrument periods (typically 10 periods of 12 s duration each). These rates are as follows: FSR (front rate, counting ToF start pulses), DCR (double coincidence rate, counting stop pulses with corresponding start pulse), MSS (main solid state detector rate, counting energy measurement pulses), and TCR (triple coincidence rate, counting energy measurement pulses with corresponding DCR pulse).

A numerical model of the sensor rates was then constructed to fit the calibration data and to extend their range to energies where no calibration could be made, and to ions which could not be calibrated, such as Si or Fe. Consider the following system of equations:

$$\text{FSR} = I_0 p_1, \quad (\text{A35a})$$

$$\text{RSR} = I_0 p_2, \quad (\text{A35b})$$

$$\text{MSS} = I_0 p_3, \quad (\text{A35c})$$

$$\text{DCR} = I_0 p_1 p_2, \quad (\text{A35d})$$

$$\text{TCR} \simeq I_0 p_1 p_2 p_3. \quad (\text{A35e})$$

I_0 is the rate of ions entering the sensor (by comparing I_0 to the calibration beam flux, the sensor geometry factor may be obtained), and p_i are the detection probabilities of the start pulse, the stop pulse, and the energy measurement, respectively. By inverting this system (equations (A35a)–(A35e)), the unknowns I_0 and p_i may be obtained. However, two difficulties arise: The last equation (equation (A35e)) is only approximate, since p_2 and p_3 are not strictly independent, and their product accounts twice for those ions being scattered away and not producing a stop signal (RSR) nor an energy signal (MSS). We still had to use (A35e) because of the second difficulty, namely, the fact that the RSR (equation (A35b)) is unavailable from the data. This has been caused in the early design phase of SWICS, owing to very severe restrictions in weight and power consumption. The inversion is still possible without (A35b), using the approximation (A35e), and it yields

$$I_0 = \frac{\text{MSS DCR}}{\text{TCR}}, \quad (\text{A36a})$$

$$p_1 = \frac{\text{FSR TCR}}{\text{MSS DCR}}, \quad (\text{A36b})$$

$$p_2 = \text{DCR/FSR}, \quad (\text{A36c})$$

$$p_3 = \text{TCR/DCR}. \quad (\text{A36d})$$

However, this system is not usable at energies below the MSS threshold, since then both TCR and MSS are zero, rendering equations (A36a–A36b) singular (but note that p_2 can still be accurately calculated from (A36c)).

The model calculates the following quantities for each element as a function of total energy (incident energy plus postacceleration):

1. The energy loss in the carbon foil ($2.5 \mu\text{g cm}^{-2}$ thickness), calculated according to Ziegler et al. [1985].
2. The probability p_1 for the ion to produce secondary electron(s) in the carbon foil, and to detect these electrons in

the start MCP. The mean number of emitted electrons, $\mu_{e,C}$, is assumed proportional to the stopping power in carbon, dE/dx again calculated according to Ziegler *et al.* [1985], at the energy with which the ion leaves the foil. The proportionality factor, C_1 , is a freely disposable parameter of the model. The probability p_1 is then calculated as the integral of a Poisson distribution around $\mu_{e,C}$ above a fixed threshold of 1.5 electrons.

3. Scattering of the ions after the carbon foil, as estimated from scattering data taken with the Karbon Folien Kollisions Analysator (KAFKA) experiment [Oetliker, 1989] and from Stopping and Ranges of Ions in Matter (SRIM) simulations [Ziegler *et al.*, 1985]. This determines the fraction of ions actually hitting the solid state detector (SSD).

4. Probability p_2 for ions to hit the SSD (see above), to produce secondary electron(s) there, and to detect these electrons in the stop MCP. Apart from the first factor, p_2 is calculated as p_1 above but with the stopping power of gold instead of carbon (since the SSD is gold coated), and with a different proportionality factor, C_2 , which is the second freely disposable parameter of the model.

5. Probability p_3 of the ions to trigger the solid state detector. Ideally, as a function of energy, this would be a step function from 0 to 1 at the detector threshold of 40 keV, but taking into account the electronic noise as well as the nuclear defect and straggling [Ipavich *et al.*, 1978], this step function is washed out to an upturn from 0 to 1, which is rather steep for light elements, but becomes more gradual for heavier species.

The model results are then compared to the calibration data for each calibrated element as a function of energy per nucleon, and the constants C_1 and C_2 are tuned in an iterative scheme, until satisfactory agreement is reached, particularly, in the expected energy range of the solar wind ions of $\sim 12 \text{ keV amu}^{-1}$ (mostly from the postacceleration by a potential drop of 23 kV); they are given as dashed lines in Figure A4. For those elements that were not available in the calibration facility, such as Si and Fe, model efficiencies are calculated using parameters C_1 and C_2 estimated from the calibrated elements by a simple linear interpolation with the mass number as the independent variable.

Finally, the efficiency used in (1) and (A22) for solar wind ions measured in triple coincidence is simply the product $\eta = p_1 p_2 p_3$ of the three probabilities that have been calculated and stored in a lookup table for each element.

Acknowledgments. We are grateful to the many individuals at the University of Maryland, the University of Bern, the Max-Planck-Institut für Aeronomie in Lindau, and the Technische Universität Braunschweig who have developed, fabricated, and calibrated the SWICS instrument. We also thank D. J. McComas for providing the SWOOPS proton speed data. This work was initiated and largely carried out when one of us (R.v.S.) was a visiting research scientist at the University of Michigan, whose support is gratefully acknowledged. N.A.S., L.A.F., G.G., S.H., and T.H.Z. were supported, in part, by NASA contracts NAG5-2810, NAG5-

7111, and JPL contract 955460. N.A.S. and T.H.Z. were also supported, in part, by NASA grant NAG5-6471 and NSF grant ATM 9714070. N.A.S. was also supported, in part, by the International Space Science Institute (ISSI). R.F.W.S. was supported, in part, by the Swiss National Science Foundation.

Janet G. Luhmann thanks Eberhard S. Möbius, David J. McComas, and two other referees for their assistance in evaluating this paper.

References

- Aellig, M. R., et al., Iron freeze-in temperatures measured by SOHO/CELIAS/CTOF, *J. Geophys. Res.*, **103**, 17,215–17,222, 1998.
- Anders, E., and N. Grevesse, Abundances of the elements: Meteoritic and solar, *Geochim. Cosmochim. Acta*, **53**, 197–214, 1989.
- Arnaud, M., and J. Raymond, Iron ionization and recombination rates and ionization equilibrium, *Astrophys. J.*, **398**, 394–406, 1992.
- Arnaud, M., and R. Rothenflug, An updated evaluation of recombination and ionization rates, *Astron. Astrophys. Suppl.*, **60**, 425–457, 1985.
- Bame, S. J., D. J. McComas, B. L. Barraclough, J. L. Phillips, K. J. Sofaly, J. C. Chavez, B. E. Goldstein, and R. K. Sakurai, The Ulysses solar wind plasma experiment, *Astron. Astrophys. Suppl.*, **92**, 237–265, 1992.
- Bochsler, P., J. Geiss, and S. Kunz, Abundances of carbon, oxygen and neon in the solar wind during the period from August 1978 to June 1982, *Sol. Phys.*, **102**, 177–201, 1986.
- Bürgi, A., Effects of non-Maxwellian electron velocity distribution functions and nonspherical geometry on minor ions in the solar wind, *J. Geophys. Res.*, **92**, 1057–1066, 1987.
- Bürgi, A., and J. Geiss, Helium and minor ions in the corona and solar wind: Dynamics and charge states, *Sol. Phys.*, **103**, 347–383, 1986.
- Feldman, U., FIP effect in the upper solar atmosphere: Spectroscopic results, *Space Sci. Rev.*, **85**, 227–240, 1998.
- Feldman, W. C., J. R. Asbridge, S. J. Bame, E. E. Fenimore, and J. T. Gosling, The solar origin of solar interstream flows: Near equatorial coronal streamers, *J. Geophys. Res.*, **86**, 5408–5416, 1981.
- Fisk, L. A., N. A. Schwadron, and T. H. Zurbuchen, Acceleration of the fast solar wind by the emergence of new magnetic flux, *J. Geophys. Res.*, **104**, 19,765–19,772, 1999a.
- Fisk, L. A., T. H. Zurbuchen, and N. A. Schwadron, On the coronal magnetic field: Consequences of large-scale motions, *Astrophys. J.*, **521**, 868–877, 1999b.
- Galvin, A. B., F. M. Ipavich, G. Gloeckler, R. von Steiger, and B. Wilken, Silicon and oxygen charge state distributions and relative abundances in the solar wind measured by SWICS on Ulysses, in *Solar Wind Seven, COSPAR Colloq. Ser.*, vol. 3, edited by E. Marsch and R. Schwenn, pp. 337–340, Pergamon, Tarrytown, N.Y., 1992.
- Galvin, A. B., R. von Steiger, and C. M. S. Cohen, Temperature asymmetry between the south and north polar coronal holes observed by SWICS/Ulysses in 1993–96 (abstract), *Eos Trans. AGU*, **78** (46), Fall Meet Suppl., F548, 1997.
- Geiss, J., Processes affecting abundances in the solar wind, *Space Sci. Rev.*, **33**, 201–217, 1982.
- Geiss, J., and G. Gloeckler, Abundances of deuterium and helium-3 in the protosolar cloud, *Space Sci. Rev.*, **84**, 239–250, 1998.

- Geiss, J., F. Bühler, H. Cerutti, P. Eberhardt, and C. Filleux, Solar wind composition experiment, in *Apollo-16 Preliminary Science Report*, chap. 14, NASA Spec. Pub. SP, NASA-SP 315, 1–10, 1972.
- Geiss, J., G. Gloeckler, and R. von Steiger, Solar and heliospheric processes from solar wind composition measurements, *Philos. Trans. R. Soc. London Ser. A*, 349, 213–226, 1994a.
- Geiss, J., R. von Steiger, G. Gloeckler, and A. B. Galvin, The neon abundance in the solar wind measured by SWICS on Ulysses (abstract), *Eos Trans. AGU*, 75 (16), Spring Meet. Suppl., S278, 1994b.
- Geiss, J., G. Gloeckler, and R. von Steiger, Origin of the solar wind from composition data, *Space Sci. Rev.*, 72, 49–60, 1995a.
- Geiss, J., et al., The southern high speed stream: Results from the SWICS instrument on Ulysses, *Science*, 268, 1033–1036, 1995b.
- Ghielmetti, A. G., H. Balsiger, R. Bänninger, P. Eberhardt, J. Geiss, and D. T. Young, Calibration system for satellite and rocket-borne ion mass spectrometers in the energy range from 5 eV/q to 100 keV/q, *Rev. Sci. Instrum.*, 54, 425–436, 1983.
- Gliem, F., W. Rieck, and H. Dinse, SWICS DPU, technical report, Inst. für Datenverarbeitungsanlagen, Thech. Univ. Braunschweig, Braunschweig, Germany, 1988.
- Gloeckler, G., A versatile detector system to measure the charge states, mass compositions and energy spectra of interplanetary and magnetosphere ions, *Tech. Rep. TR77-043*, Univ. of Maryland, College Park, 1977.
- Gloeckler, G., and J. Geiss, Measurement of the abundance of helium-3 in the Sun and in the local interstellar cloud with SWICS on Ulysses, *Space Sci. Rev.*, 84, 275–284, 1998a.
- Gloeckler, G., and J. Geiss, Interstellar and inner source pickup ions observed with SWICS on Ulysses, *Space Sci. Rev.*, 86, 127–159, 1998b.
- Gloeckler, G., and K. C. Hsieh, Time-of-flight technique identification at energies from 2 to 400 keV/nucleon, *Nucl. Instrum. Methods*, 165, 537–, 1979.
- Gloeckler, G., F. M. Ipavich, D. C. Hamilton, B. Wilken, and G. Kremser, Heavy ion abundances in coronal hole solar wind flows (abstract), *Eos Trans. AGU*, 70, 424, 1989.
- Gloeckler, G., et al., The Solar Wind Ion Composition Spectrometer, *Astron. Astrophys. Suppl.*, 92, 267–289, 1992.
- Gloeckler, G., et al., Investigation of the composition of solar wind and interstellar matter using solar wind and pickup ion measurements with SWICS and SWIMS on the ACE spacecraft, *Space Sci. Rev.*, 86, 497–539, 1998.
- Gosling, J. T., S. J. Bame, D. J. McComas, J. L. Phillips, A. Balogh, and K. T. Strong, Coronal mass ejections at high heliographic latitudes: Ulysses, *Space Sci. Rev.*, 72, 133–136, 1995.
- Grevesse, N., and A. J. Sauval, Standard solar composition, in *Solar Composition and Its Evolution – From Core to Corona*, *Space Sciences Series of ISSI*, vol. 5, edited by C. Fröhlich et al., pp. 161–174, Kluwer Acad., Norwell, Mass., 1998.
- Hefti, S., Solar wind freezing-in temperatures and fluxes measured with SOHO/CELIAS/CTOF and calibration of the CELIAS sensors, Ph. D. thesis, Univ. Bern, Bern, 1997.
- Hollweg, J. V., Some physical processes in the solar wind, *Rev. Geophys.*, 16, 689–720, 1978.
- Hovestadt, D., et al., CELIAS – charge, element and isotope analysis system for SOHO, *Sol. Phys.*, 162, 441–481, 1995.
- Hundhausen, A. J., Physics and Chemistry in Space, vol. 5, *Coronal Expansion and Solar Wind*, Springer-Verlag, New York, 1972.
- Hundhausen, A. J., Nonlinear model of high-speed solar wind streams, *J. Geophys. Res.*, 78, 1528–1542, 1973.
- Ip, W.-H., and W. I. Axford, On the first ionization potential effect in the solar corona, *Adv. Space Res.*, 11 (1), 247–250, 1991.
- Ipavich, F. M., R. A. Lundgren, B. A. Lambird, and G. Gloeckler, Measurements of pulse-height defect in Au-Si detectors for H, He, C, N, O, Ne, Ar, Kr from 2 to 400 keV/amu, *Nucl. Instrum. Methods*, 154, 291–294, 1978.
- Ipavich, F. M., A. B. Galvin, J. Geiss, K. W. Ogilvie, and F. Gliem, Solar wind iron and oxygen charge states and relative abundances measured by SWICS on Ulysses, in *Solar Wind Seven, COSPAR Colloq. Ser.*, vol. 3, edited by E. Marsch and R. Schwenn, pp. 369–374, Pergamon, Tarrytown, N. Y., 1992.
- Ko, Y.-K., L. A. Fisk, J. Geiss, G. Gloeckler, and M. Guhathakurta, An empirical study of the electron temperature and heavy ion velocities in the south polar coronal hole, *Sol. Phys.*, 171, 345–361, 1997.
- Krieger, A. S., A. F. Timothy, and E. C. Roelof, A coronal hole and its identification as the source of a high velocity solar wind stream, *Solar Phys.*, 29, 505–525, 1973.
- Marsch, E., R. von Steiger, and P. Bochsler, Element fractionation by diffusion in the solar chromosphere, *Astron. Astrophys.*, 301, 261–276, 1995.
- McKenzie, J. F., M. Banaszkiewicz, and W. I. Axford, Acceleration of the high speed solar wind, *Astron. Astrophys. Lett.*, 303, L45–L48, 1995.
- Neukomm, R. O., Composition of coronal mass ejections derived with SWICS/Ulysses, Ph. D. thesis, Univ. Bern, Bern, 1998.
- Oetliker, M., Charge state distribution, scattering, and residual energy of ions after passing through thin carbon foils, M. S. thesis, Univ. Bern, Bern, 1989.
- Oetliker, M., CTOF, a solar wind time-of-flight mass spectrometer with high charge resolution: Numerical simulations and calibrations, Ph. D. thesis, Univ. Bern, Bern, 1993.
- Peter, H., Velocity-dependent fractionation in the solar chromosphere, *Astron. Astrophys.*, 312, L37–L40, 1996.
- Rosenbauer, H., R. Schwenn, E. Marsch, B. Meyer, H. Miggenrieder, M. D. Montgomery, K. H. Mühlhäuser, W. Pilipp, W. Voges, and S. M. Zink, A survey on initial results of the Helios plasma experiment, *J. Geophys.*, 42, 561–580, 1977.
- Schwadron, N. A., L. A. Fisk, and T. H. Zurbuchen, Elemental fractionation in the slow solar wind, *Astrophys. J.*, 521, 859–867, 1999.
- Schwenn, R., Large-scale structure of the interplanetary medium, in *Physics of the Inner Heliosphere*, vol. 1, edited by R. Schwenn and E. Marsch, chap. 3, pp. 99–181, Springer-Verlag, New York, 1990.
- Steinacher, M., F. Jost, and U. Schwab, A modern and fully automated calibration system for space ion mass spectrometers, *Rev. Sci. Instrum.*, 66, 4180–4187, 1995.
- Vauclair, S., Element segregation in the solar chromosphere and the FIP bias: The “skimmer” model, *Astron. Astrophys.*, 308, 228–232, 1996.
- von Steiger, R., Composition of the solar wind, habilitation thesis, Univ. Bern, Bern, 1995.
- von Steiger, R., Composition aspects of the upper solar atmosphere, in *Solar Composition and Its Evolution – From Core to Corona*, *Space Sciences Series of ISSI*, vol. 5, edited by C. Fröhlich et al., pp. 407–418, Kluwer Acad., Norwell, Mass., 1998.
- von Steiger, R., and J. Geiss, Supply of fractionated gases to the corona, *Astron. Astrophys.*, 225, 222–238, 1989.
- von Steiger, R., S. P. Christon, G. Gloeckler, and F. M. Ipavich, Variable carbon and oxygen abundances in the solar wind as observed in Earth’s magnetosheath by AMPTE/CCE, *Astrophys. J.*, 389, 791–799, 1992.

- von Steiger, R., J. Geiss, and G. Gloeckler, Composition of the solar wind, in *Cosmic Winds and the Heliosphere*, edited by J. R. Jokipii, C. P. Sonett, and M. S. Giampapa, pp. 581–616, Univ. of Ariz. Press, Tucson, 1997.
- Wenzel, K.-P., R. G. Marsden, D. E. Page, and E. J. Smith, The Ulysses mission, *Astron. Astrophys.*, *92*, 207–219, 1992.
- Wieler, R., The solar noble gas record in lunar samples and meteorites, *Space Sci. Rev.*, *85*, 303–314, 1998.
- Wimmer-Schweingruber, R. F., Oxygen, helium, and hydrogen in the solar wind: SWICS/Ulysses results, Ph. D. thesis, Univ. of Bern, Bern, 1994.
- Wimmer-Schweingruber, R. F., R. von Steiger, and R. Paerli, Solar wind stream interfaces in corotating interaction regions: New SWICS/Ulysses results, *J. Geophys. Res.*, *104*, 9933–9945, 1999.
- Ziegler, J. F., J. P. Biersack, and U. Littmark, *The Stopping and Range of Ions in Solids*, vol. 1, Pergamon, Tarrytown, N. Y., 1985.
- L. A. Fisk, S. Hefti, N. A. Schwadron, and T. H. Zurbuchen, Department of Atmospheric, Oceanic and Space Sciences, University of Michigan, 2455 Hayward St., Ann Arbor, MI 48109.
- J. Geiss and R. von Steiger, International Space Science Institute, Hallerstrasse 6, CH-3012 Bern, Switzerland. (vsteiger@issi.unibe.ch)
- G. Gloeckler, Department of Physics, University of Maryland, College Park, MD 20742.
- B. Wilken, Max-Planck-Institut für Aeronomie, Postfach 20, D-37189 Katlenburg-Lindau, Germany.
- R. F. Wimmer-Schweingruber, Physikalisches Institut, University of Bern, Sidlerstrasse 5, CH-3012 Bern, Switzerland.

September 27, 1999; revised July 5, 2000; accepted July 5, 2000.

This preprint was prepared with AGU's \LaTeX macros v4, with the extension package 'AGU⁺⁺' by P. W. Daly, version 1.6 from 1999/02/24.